DOI: 10.1070/RCR4849

Physicochemical phenomena leading to slip of a fluid along a solid surface

Alexander Ya. Malkin,[a] Stanislav A. Patlazhan,[b] Valerii G. Kulichikhin [a]

[a] A.V.Topchiev Institute of Petrochemical Synthesis, Russian Academy of Sciences Leninsky prosp. 29, 119991 Moscow, Russian Federation
[b] Semenov Institute of Chemical Physics, Russian Academy of Sciences ul. Kosygina 4, 119991 Moscow, Russian Federation

The aim of the review is to analyze theoretical approaches to the explanation of the phenomenon of slip of different media including homogeneous fluids and multicomponent systems, such as pastes, microgels, concentrated suspensions, highly concentrated emulsions and polymer melts along solid walls. The wall slip conditions and physical mechanisms are considered. The influence of molecular interactions of homogeneous fluids and disperse systems with hydrophobic and hydrophilic solid surfaces, as well as the role of surface roughness, nanobubbles, deformation-induced relaxation transition from liquid to solid-like behaviour of viscoelastic polymers in the course of slip are demonstrated. Key results of experimental studies are discussed.
The bibliography includes 296 references.

Contents

1. Introduction 319
2. Slip of homogeneous fluids. The wettability and structure of surface 322
3. Interaction of multicomponent fluids with solid wall 332
4. Polymer melts 339
5. Conclusion 345

1. Introduction

Problems associated with understanding the causes for slip of a flowing fluid along a solid wall are interdisciplinary. Assessment of the behaviour of a fluid at the interface is necessary when solving fluid dynamics boundary value problems that are formulated as the momentum equations (Navier – Stokes equations) irrespective of the rheological properties of fluids. Generally, answers are ambiguous and depend on the physicochemical processes occurring at the fluid/solid interface. A conventional assumption of zero relative velocity at the solid surface, which underlies solution of numerous hydrodynamic problems including the Hagen – Poiseuille equation,[1,2] is no more than a convenient assumption. Simplicity of the answer was repeatedly discussed in scientific literature. Noteworthy, Claude-Louis Navier, the founder of the classical dynamics of viscous fluids, also participated in those discussions. Navier believed that a fluid near a solid wall exhibits specific properties and introduced the notion 'slip length' (l) to describe them. Since then the slip length has been the main quantitative characteristic of the wall effects related to the slip of a fluid relative to fixed solid wall.[3]

The slip length is directly related to the slip velocity of the fluid along a solid wall (V_w) and to the corresponding shear rate at the channel wall ($\dot{\gamma}_w$) by a simple relation:

A.Ya.Malkin. Doctor of Sciences (Physics and Mathematics), Professor, Principal Researcher at the TIPS RAS.
Telephone: +7(495)954 – 4320, e-mail: alex_malkin@mig.phys.msu.ru
Current research interests: rheology, mechanics and physical chemistry of polymers and colloidal systems, flow instability of viscoelastic media, composite materials, nanosystems, rheokinetics of chemical and physical processes, polymer processing and technology.
S.A.Patlazhan. Doctor of Sciences (Physics and Mathematics), Professor, Principal Researcher at the ICP RAS.
Telephone: +7(495)939 – 7177, e-mail: sapat@yandex.ru
Current research interests: physicochemical hydrodynamics of polymer fluids, structure-sensitive mechanics and rheology of microheterogeneous polymer materials, self-organizing polymer materials.
V.G.Kulichikhin. Corresponding Member of the Russian Academy of Sciences, Doctor of Sciences (Chemistry), Professor, Head of Laboratory at the TIPS RAS.
Telephone: +7(495)955 – 4235, e-mail: klch@icp.ac.ru
Current research interests: physical chemistry and rheology of polymers, colloid chemistry, nanocomposites, fibre spinning, liquid-crystalline polymers.

Received 26 June 2018
Translation: A.M.Raevskiy

© 2019 Uspekhi Khimii, Russian Academy of Sciences and Turpion Ltd.

$$l = \frac{V_w}{\dot{\gamma}_w} \tag{1}$$

Note that for simple shear flow $\dot{\gamma}_w$ equals the basic shear rate ($\dot{\gamma}$). The shear stress at the wall (σ_w) is related to the slip velocity, the coefficient of proportionality being equal to the friction coefficient (κ)

$$\sigma_w = \eta\dot{\gamma}_w = \kappa V_w \tag{1a}$$

The slip length can also be expressed as:

$$l = \frac{\eta}{\kappa} \tag{2}$$

where η is the viscosity of the fluid.

From relationships (1) and (2) it follows that the slip length is not an absolute characteristic of the boundary conditions, but is expressed through two parameters that characterize the properties of the surface (friction coefficient κ) and the bulk properties of the fluid (viscosity η), which can generally be velocity- or stress-dependent.[4–6]

The definition of the slip length under simple shear can be illustrated geometrically. One has to determine the position of the intersection point of the linear dependence $V(y)$ extrapolated to $V = 0$ with the axis coinciding with the channel wall. Having determined this position, we get the slip velocity V_w (Fig. 1 *a*). However, this formal method gives no particular values of the slip velocity since, first, the slip length can be small compared to the size of the channel cross-section. Next, the velocity profile can be nonlinear, in particular, due to the formation of a thin layer of the fluid whose viscosity is much lower than the bulk viscosity, $\eta_w \ll \eta$.[5,6] Then, linear extrapolation cannot be used because the velocity profile near the wall becomes curved and eventually the slip velocity at the wall can be zero. In this case it seems reasonable to assess the apparent slip length l_{app} (Fig. 1 *b*);[7] the shear rate gradient increases owing to formation of a lubricating layer. The shear stress at the wall is given by[7]

$$\sigma_w = \frac{\eta_w V_w}{\delta} \tag{3}$$

and the apparent slip length is

$$l_{app} \approx \delta\frac{\eta}{\eta_w} \tag{3a}$$

where δ is the thickness of the thin near-wall layer of the fluid.

A direct experimental proof of the wall slip effects is provided by the dependence of the effective viscosity calculated by conventional methods of continuum mechanics using the no-slip hypothesis as the boundary condition on the geometric parameters of the channel. For instance, the dependence of the viscosity determined from the Hagen–Poiseuille equation on the diameter of a capillary may be indicative of a wall slip.

The first experimental observations that demonstrated the possibility for fluids to undergo wall slip were reported in the 1930s (Ref. 8) while the key theoretical estimates were obtained by Tolstoi,[9] Churaev *et al.*[10] and Blake.[11] Having mentioned these pioneering publications, we will not dwell on numerous earlier and more recent experimental and theoretical studies on the slip of fluids across solid surfaces because a number of relevant reviews are available.[12–14]

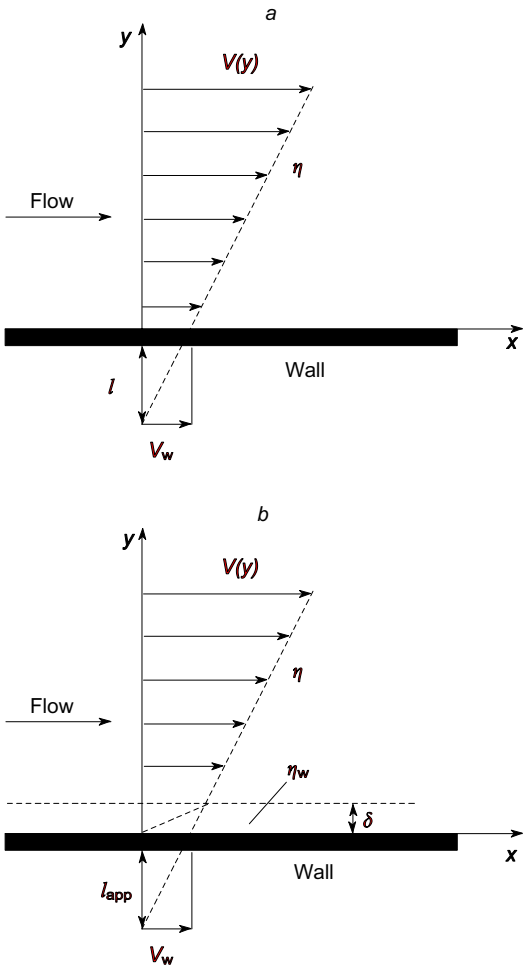


Figure 1. Flow velocity profiles for true wall slip (*a*) and for apparent slip assuming the formation of a near-wall layer of low-viscous fluid (*b*).[7]

The problem of slip of fluids across solid surfaces still remains at the focus of modern physics and physical chemistry of surface phenomena. Recent studies in the field have been reviewed.[15–18] The reasons for incessant attention to this avenue of research are as follows:

— interest in the surface phenomena that arise due to the absence of or insufficient wetting of the solid surface; related effects are of particular importance in connection with the design of hydrophilic or lyophilic surfaces;

— interest in flow through microcapillaries, especially if the size of the channel is comparable with the free path length of Brownian motion; corresponding problems become crucially important owing to progress in microfluidics; besides, accompanying phenomena are of importance for such media as physiological fluids, in particular, blood;

— interest in the flow of multicomponent systems where their motion is accompanied by changes in the spatial distribution of components. In some cases this causes the formation of a thin surface layer with specific properties that differ from the bulk properties of the medium; this is

accompanied by the onset of apparent slip since the viscosity of the thin layer is much lower than the bulk viscosity of the system, and the shear rate near the solid surface much exceeds the average bulk shear rate;

— interest in flow of viscoelastic fluids whose relaxation properties depend on the rate of deformation, since in certain cases one deals with a deformation-induced flow – rubbery relaxation-type transition of the material and, as a consequence, continuous or periodic relaxation slip across the solid surface.

The text below is based on this background.

The aim of this review is to classify the results of present-day research into the slip of fluids across solid surfaces in order to reveal basic mechanisms of the observed phenomena. Earlier studies in the field will be mentioned only if they are historically important or are key to certain problems in question. Besides, we will dwell on some moot questions touched in the previously published reviews.

This publication is organized as follows. First, we briefly outline the theoretical basis and the approaches that explain the possibility for fluids to slip across solid boundary surfaces taking into account the interaction of simple fluids with hydrophilic (hydrophobic) surfaces of different roughness. Next, we will consider two main types of fluids,, *viz*., multicomponent dispersions (including colloidal systems) and polymer melts, as well as possible manifestations of the slip of these media across solid surfaces.

Notations are as follows:

γ — surface tension;
$\dot{\gamma}$ — basic shear rate;
$\dot{\gamma}_c$ — critical shear rate;
$\dot{\gamma}_w$ — shear rate at solid wall;
δ — thickness of a thin layer of fluid near solid wall;
δ^* — sagging depth of fluid meniscus;
ε — depth of a potential well;
ε_{ik} — Lennard-Jones interaction potential;
ε_e — elastic deformation;
ε_f — flow deformation;
ζ — deformation of spherical particle;
η — fluid viscosity;
η_s — solvent viscosity;
η_w — viscosity of thin near-wall fluid layer;
η_0 and η_∞ — limiting viscosity at zero and infinitely high shear rate, respectively;
θ — wetting angle;
θ_{CB} and θ_W — wetting angles of rough surface in Cassie – Baxter and Wenzel states, respectively;
θ_{pr} and θ_c — bubble protrusion angle and critical bubble protrusion angle, respectively;
θ_Y — Young wetting angle of smooth surface;
κ — friction coefficient;
λ_g — mean free path of gas molecules;
λ, n and a — parameters of Carreau – Yasuda model;
v — approach velocity of solid surfaces;
v_z — average normal component of molecular velocity for gas;
ρ_w — density of the contact layer of fluid at solid wall;
ρ_g, ρ_f and ρ_s — density of gas, fluid and solid substrate, respectively;
σ — shear stress;
σ_b — flow breakdown stress;
σ_c — critical shear stress;
σ_s — slip threshold;
σ_p — elastic stress of particle;
σ_y — yield stress;
σ_w — shear stress at channel wall;
ϕ — volume fraction of polymer and disperse phase;
ϕ_{max} — maximum packing fraction of solid particles;
φ — surface fraction of fluid/gas interface;
φ_s — surface fraction of solid protrusions;
ψ — elasticity parameter of soft particles;
ω — frequency;
Ω — contact surface area;
A — roughness amplitude;
b — Kuhn segment length;
B and K — compression and flexural moduli of a membrane, respectively;
c_{fs} — fluid – solid interaction parameter (strength);
d_f — fractal dimension;
D_p — capillary diameter;
$D_{q||}$ — collective diffusion coefficient;
DEP — diethyl phthalate;
f^* — factor;
F_x — tangential component of total force;
F_h — hydrodynamic force;
F_{St} — Stokes' frictional force (Stokes' drag);
G — elastic modulus of amorphous polymers;
G_0 — shear modulus of dispersion;
G_p — elastic modulus of spherical particle;
h — distance between solid surfaces;
k — Bolzmann constant;
Kn — Knudsen number;
l — slip length;
l_{app} — apparent slip length;
l_{eff} — effective slip length;
$l_{eff,||}$ and $l_{eff,\perp}$ — effective slip length along and transverse stripe texture;
$l_{W,||}$ — effective longitudinal slip length of Newtonian fluid in the Wenzel regime;
l^- and l^+ — local slip length of nonuniform surface;
L — roughness period and superhydrophobic texture period;
L_p — capillary length;
MD — molecular dynamics;
MMD — molecular mass distribution;
$\mathbf{n}$ — unit normal vector;
N — degree of polymerization;
N_1 — first difference of normal stresses;
p — fluid pressure;
p_0 — pressure in a thin film near solid wall;
P_{ch} and P_g — fluid pressure in channel and in gas-filled grooves, respectively;
ΔP — pressure drop along the capillary;
PAA — polyacrylamide;
PS — polystyrene;
$q_{||}$ — reciprocal lattice vector of solid substrate;
q — electrostatic charge of polymer jet;
Q — volumetric flow rate of a fluid;
r_0 — flat face radius of deformed particle;
r_f — degree of surface roughness;
r_s — distance from average heigth of protrusions to virtual level;
R — radius of a cylinder;
t — time;
T — absolute temperature;
$\mathbf{u}(x, y)$ — local flow velocity vector;
$\langle\mathbf{u}\rangle$ — average flow velocity;
$\mathbf{u}'(x, y)$ — flow velocity perturbation field;

U — channel wall velocity;
$V(y)$ — velocity profile;
V_p — central plug velocity in the plug flow profile;
V_y — slip velocity at yield stress;
V_w — fluid slip velocity at solid wall;
Wi — Weissenberg number;
Wi_c — critical Weissenberg number;
w_g and $w = w_g/L$ — dimensional and dimensionless groove width, respectively.
y_{max} — normal coordinate of zero flow velocity.

2. Slip of homogeneous fluids. The wettability and structure of surface

In this Section we will consider the role of the key factors, first of all, wettability and structure of solid boundary surfaces, as well as near-wall nano- and microbubbles that specify the conditions for the onset of wall slip of homogeneous fluids. At present, this is of particular importance in connection with the design of superhydrophobic surfaces.

2.1. The nature of slip

The nature of slip of a fluid on a nonwettable solid surface was for the first time considered by Tolstoi.[9] According to his model, slip becomes possible when the energy accumulated by the fluid at the interface becomes high enough to form a microcavity. According to calculations for mercury flow in glass capillary, slip becomes noticeable for capillaries at most 10 μm in diameter. The possibility of water slip in microscopic capillaries with hydrophobic walls was reported in another study.[10]

The boundary conditions between the fluid and the solid surface, as well as physical mechanisms of wall slip depend on many factors including the molecular mass of the fluid, the interaction energy of the fluid with the solid substrate, the roughness of the substrate surface, the presence of bubbles at the interface, the kinetics of gas liberation (or dissolution) in the liquid phase, fluid structuring near the solid wall, *etc*.

Among the first attempts to relate the boundary conditions for slip of a fluid to the molecular characteristics of the fluid and wettability of the solid surface, there are two studies by Bocquet and Barrat.[4, 19] They consider the Lennard-Jones potential (ε_{ik}) of pair interaction between fluid molecules ($i = k$ = f) and between fluid molecules (i = f) and the solid phase molecules (k = s) at the same depth (ε) and diameter (d) of the potential well

$$\varepsilon_{ik} = 4\varepsilon\left[\left(\frac{d}{r}\right)^{12} - c_{ik}\left(\frac{d}{r}\right)^{6}\right] \tag{4}$$

where r is the intermolecular distance. The surface energy (ε_{fs}) was determined by varying the fluid – substrate interaction coefficient c_{fs}, and the friction coefficient κ between the fluid and substrate was specified by the Green – Kubo expression:

$$\kappa = \frac{1}{kT\Omega}\int_0^\infty \langle F_x(t)\, F_x(0)\rangle \mathrm{d}t \tag{5}$$

where k is the Boltzmann constant, T is absolute temperature, Ω is the contact surface area, F_x is the tangential component of the total force exerted by the flowing fluid on the interface and t is time. It was found[19] that the slip length (l) is inversely proportional to the squared coefficient c_{fs}

$$l \sim \frac{\eta D_{q_{||}}}{c_{fs}^2 \rho_w S_{q_{||}}} \tag{6}$$

where $D_{q||}$ and $S_{q||}$ are respectively the collective diffusion coefficient and the structural factor of the fluid ($q_{||}$ is the reciprocal lattice vector of the solid crystalline substrate), ρ_w is the density of the fluid contact layer at the solid wall. From Laplace's estimate of surface energy [20]

$$\gamma_{fs} = -\rho_f \rho_s \int_{r_0}^{\infty} r\, \varepsilon_{fs}(r)\mathrm{d}r \tag{7}$$

and Young's law it was found that the Young wetting angle (θ_Y) can be described as follows:[19]

$$\cos\theta_Y = -1 + \frac{2\rho_s c_{fs}}{\rho_f c_{ff}} \tag{8}$$

where ρ_s and ρ_f are the bulk densities of the solid substrate and fluid, respectively, and c_{ff} is the Lennard-Jones parameter for the interaction between fluid molecules.

From relations (6) and (8) it follows that at low interaction energy between the fluid and the solid surface ($c_{fs} \ll c_{ff}$), the wetting angle θ_Y and the slip length l noticeably increase. In particular, at $c_{fs} \to 0$, the Young wetting angle approaches 180° and $l \to \infty$, thus favouring the onset of plug flow. Thus, wetting and slip of a fluid on a solid surface are interrelated. This was confirmed by the results of molecular dynamics (MD) simulations.[19, 21] Moreover, a numerical simulation showed that the theory outlined above correctly describes changes in the slip length [expression (6)] even for polymer fluids.[22]

More detailed MD studies revealed that the slip length of a Newtonian fluid can be shear-rate dependent. For simple Newtonian fluids the slip length remains constant ($l = l_0$) only at rather low shear rates and abruptly increases near a certain critical shear rate $\dot\gamma_c$ (Fig. 2 *a*).[23] Depending on the density of thin near-surface fluid layer and on the energy of intermolecular interaction with the substrate, the l_0 value varies from 0 to a few tens of nanometres. A simulation of the flow of polymer melts also confirmed this result.[22] An increase in the degree of polymerization N was accompanied by a linear increase in the slip length l (see inset in Fig. 2 *b*),[22] while the critical shear rate is related to the energy landscape of the surface and also depends on the molecular mass of polymer chains.

It is noteworthy that the results of MD simulation of flow of low- and high-molecular-mass fluids near solid substrates fall on a master curve plotted in the coordinates $(l/l_0) - (\dot\gamma/\dot\gamma_c)$ (Fig. 3).[22] The dependence is well described by the expression [22, 23]

$$\frac{l}{l_0} = \left(1 - \frac{\dot\gamma}{\dot\gamma_c}\right)^{-1/2} \tag{9}$$

from which it follows that the slip length increases without bound at $\dot\gamma \to \dot\gamma_c$. Therefore, in the vicinity of the critical shear rate the shear stress at the wall approaches zero.

An increase in the slip length of Newtonian fluids with increasing shear rate was observed by atomic force microscopy (AFM) for both hydrophobic and hydrophilic surfa-

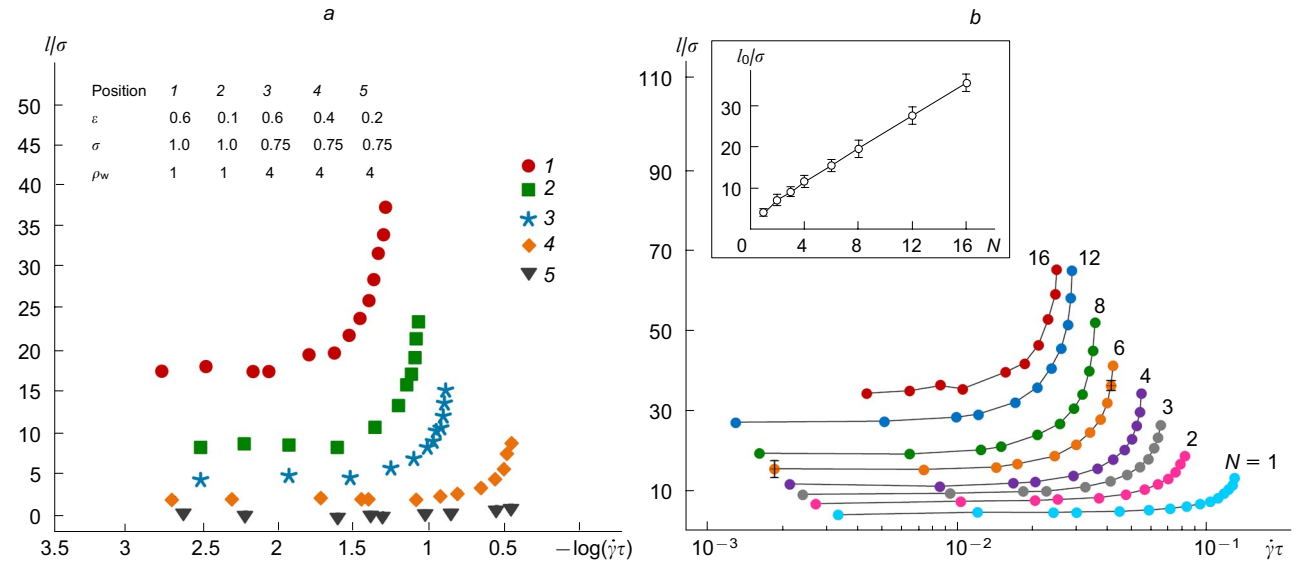


Figure 2. Slip length-*vs.*-shear rate plots for a low-molecular-mass fluid at different values of the parameters ε, d and ρ_w (*a*)[23] and for polymer melts of different degree of polymerization N (*b*).[22]
Here, $\tau = d(m/\varepsilon)^{1/2}$ is the characteristic time of the Lennard-Jones potential and m is the molecular mass.

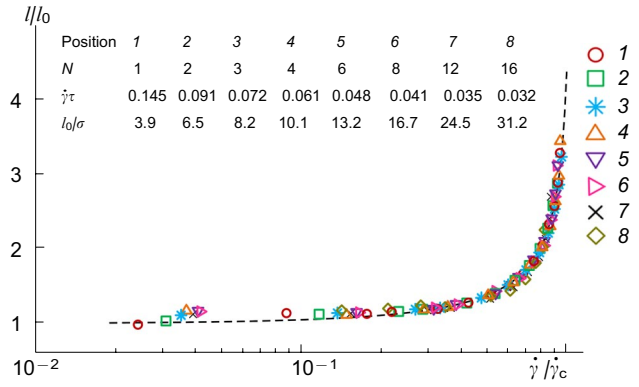


Figure 3. Relative slip length (l/l_0) plotted *vs.* relative shear rate ($\dot{\gamma}/\dot{\gamma}_c$) using data for different smooth surfaces.[22]
The dashed curve was calculated using expression (9).

ces.[24–30] An analysis of hydrodynamic forces F_h produced during normal low-frequency oscillations of crossed cylinders (of radii $R \approx 2$ cm) with smooth surfaces revealed an abnormal increase in the slip length.[24] This conclusion was drawn taking into account the deviation of the hydrodynamic force from the Reynolds law

$$F_h = F_{St} R h^{-1} \tag{10}$$

($F_{St} = 6\pi R\eta v$ is the Stokes' frictional force, v is the approach velocity of the cylinders), derived assuming no wall slip and short distances h between solid surfaces compared to R. According to the Reynolds law, a decrease in h to zero should be accompanied by unlimited increase in the compression force. However, wall slip reduces the hydrodynamic force F_h that is given by[7]

$$F_h = f^* F_{St} R h^{-1} \tag{11}$$

$$f^* = \frac{h}{3l}\left[\left(1 + \frac{h}{6l}\right)\ln\left(1 + \frac{6l}{h}\right) - 1\right] \tag{11a}$$

The factor f^* removes the singularity at $h \to 0$ while the hydrodynamic force F_h decreases as the slip length increases (see Fig. 4).[24] Experiments showed that the slip length at hydrophobic surfaces begins to increase at much lower shear rates compared to slip at hydrophilic surfaces.[24] In all cases the slip length falls on the micrometre length scale and thus much exceeds the values obtained from numerical simulations[4, 19, 21–23] and from the experiments using low-molecular-mass fluids under Couette and Poiseuille flows.[10, 11, 31, 32]

It was assumed[7, 33] that the experimentally observed abnormally large slip length can be due to the presence of a sufficiently thick gas film on the solid surface. De Gennes[33] assumed two sources of gas bubbles:

— thermal fluctuations at the solid wall; and

— external gas dissolved in the fluid.

In the former case the thickness of the gas film ('mattress') equals the thickness of the low-density fluid layer at the solid wall

$$\delta \sim \left(\frac{kT}{\gamma}\right)^{1/2} \tag{12}$$

(T is absolute temperature and γ is the surface tension) and the slip length can be as large as 15 molecular diameters; this is in agreement with the theoretical concept mentioned above[19] and with certain experimental data.[4, 34, 35] In the latter case, the friction coefficient of the fluid is proportional to the average normal component of the velocity of the molecules ($\bar{v}_z$) penetrating into the gas phase from the bulk of the fluid,

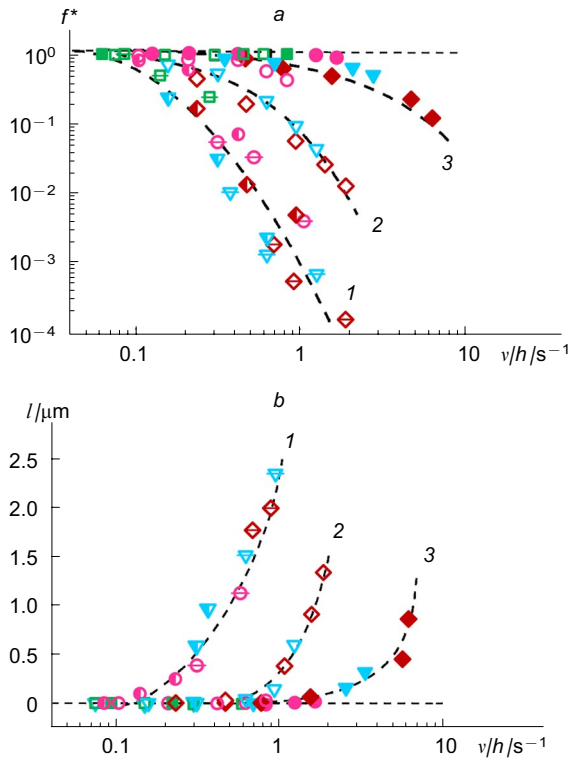


Figure 4. Parameter f^*(*a*) and the slip length, *l*, of the fluid (*b*) plotted *vs*. apparent shear rate v/h: the case of smooth cylinder surfaces.[24]
Deionized water (*1*) and tetradecane (*2*) between mica surfaces coated with octadecyltriethoxysiloxane (OTE) [θ_Y = 110° (*1*), 44° (*2*)] and tetradecane containing 0.2 mol.% hexadecylamine (*3*) between mica surfaces (θ_Y = 12°).

$$\bar{v}_z \propto \left(\frac{kT}{2\pi m}\right)^{1/2} \tag{13}$$

Then, in the approximation of large Knudsen numbers

$$\mathrm{Kn} = \frac{\lambda_g}{\delta} \gg 1 \tag{14}$$

(λ_g is the mean free path of gas molecules) for the apparent slip length [33]

$$l_{app} \approx \frac{\eta}{\rho_g \bar{v}_z} \tag{15}$$

(ρ_g is the density of the gas) can be as large as a few micrometres.[24,36] The estimate obtained by de Gennes can be represented in a more compact form [37]

$$l_{app} \approx \delta\left(2\,\mathrm{Kn}\frac{\eta}{\eta_g} - 1\right) \tag{16}$$

where η_g is the viscosity of the gas. However, this approximation is inapplicable at rather high gas densities where the Knudsen number becomes small. In this case, a more general formula [37] is valid:

$$l_{app} \approx \delta\left[\frac{1}{4}\frac{\eta}{\eta_g}\frac{(2\,\mathrm{Kn}+1)(1+6\,\mathrm{Kn})}{1+3\,\mathrm{Kn}} - 1\right] \tag{17}$$

In the limit $\mathrm{Kn} \to 0$, the results obtained using expression (17) agree with those of MD simulation and theoretical predictions.[38,39] Nevertheless, this approach gives no explanation for anomalous dependence of the slip length on the shear rate, which was observed in the experiments with vibrating crossed cylinders (see Fig. 4 *b*).[24]

2.2. Nanobubbles at fluid/solid interface

The results considered above were explained within the framework of theoretical analysis of the compression dynamics of gas nanobubbles localized at the fluid/solid interface taking account of gas diffusion into bubbles and into the surrounding liquid phase.[40] This model was termed 'leaking mattress'. It was shown that normal oscillations of solid walls initiate compression and expansion of bubbles. This leads to a decrease in the volume of the fluid displaced from the thin channel and, therefore, in the force F_h acting on the solid wall, which is due to apparent slip.

The existence of stable gas nanobubbles at the interface between water and hydrophobic surface was repeatedly confirmed by AFM.[41–51] The wall nanobubbles in low-molecular-mass fluids are from 10 to 100 nm in size,[52–54] being much larger in polymer melts (*e.g.*, hundreds of micrometres for polybutadiene on smooth silica surface covered with low-energy perfluorosilane monolayer [55]). An important factor is the lifetime of bubbles, which can vary from a few hours to weeks.[52,54,56–59] These data seemingly contradict the basic ideas of stability of gas bubbles. Indeed, the simplest estimates show that the gas pressure in the nanobubbles can be as high as 100 atm. In this case, nanobubbles should rapidly dissolve in water. In particular, mention was made that, would the Henry law be valid on the nanoscale, the nanobubble lifetime should be of the order of 1 μs.[60]

Attempts to explain the unexpectedly long lifetime of nanobubbles at the fluid/solid wall interface led to the development of some interesting theoretical approaches. In particular, it was assumed that the gas outflux from nanobubbles owing to Laplace pressure can be compensated by the influx gas in the vicinity of the contact line due to attraction of gas molecules to the hydrophobic surface (this can extend the stability of nanobubbles to a metastable equilibrium under certain conditions).[61] However, this assumption was not confirmed experimentally, *viz*., the addition of surfactants had no effect on the lifetime of nanobubbles.[62]

At the same time, it was shown [63] that the key role in the increase in the lifetime of nanobubbles at the fluid/solid surface interface can be played by the following two factors:

— pinning of the interface and

— thickness of the fluid layer above nanobubbles.

Pinning of the contact line causes the radius of curvature of bubbles to increase with time. This leads to a decrease in the Laplace pressure and, therefore, to an increase in the lifetime of nanobubbles. According to calculations, at a relatively large thickness of the fluid layer, dissolution of bubbles in the bulk of the fluid occurs a few orders of magnitude slower than near the free surface. In other words, the stability of nanobubbles has a kinetic nature.

Surface nanobubbles are usually formed as a result of condensation of gases dissolved in water at interfaces with hydrophobic solid surfaces.[41,42,46,48] A direct AFM observation of the nucleation of gas bubbles at the water/pyrolytic graphite interface showed that nanobubbles nucle-

ate upon merging of the clusters of gas molecules adsorbed on the solid surface.[50] It was established that near-wall nanobubbles have similar mechanical properties. This implies low surface tension and a liquid-like nature of nanobubbles. These conclusions were confirmed by the results of an MD simulation of the interaction of water molecules with a hydrophobic surface,[64] according to which the density of the gas in nanobubbles should be rather high (up to 300 kg m^{-3}). It is assumed that it is just this physical mechanism that is responsible for the high stability of nanobubbles.[65]

2.3. Effect of solid wall roughness on fluid slip

When analyzing experimental data, one should take account of the roughness of solid surfaces since the presence of nanoscale and microscopic asperities and troughs can require significant modification of the boundary conditions at the fluid/solid interface.[29, 30, 66 – 72] For instance, an MD simulation of shear flow of a low-molecular-mass fluid showed that the roughness of the hydrophobic wall causes a marked decrease in the slip length and leads to removal of singularity predicted for atomically smooth surface at certain critical shear rate $\dot{\gamma}_c$ (Fig. 5).[69] An increase in the roughness amplitude A and period L causes a monotonic decrease in the effective slip length of both simple and polymer fluids.[70 – 72] It was shown that polymer chains extend along the flow direction over protrusions, being oriented transverse to the flow in troughs; this changes the local viscosity of the polymer melt. It is this feature that is responsible for the deviation of the results of MD simulation from those of the solution of the Navier – Stokes equation with the Navier boundary condition (in this case, the local slip length is shear-rate dependent).[71] The results obtained qualitatively agree with the conclusion that the wave-like character of the surface relief with ideal local slip leads to dependence of the average slip velocity of a Newtonian fluid on the parameters A and L, *viz.*,[73]

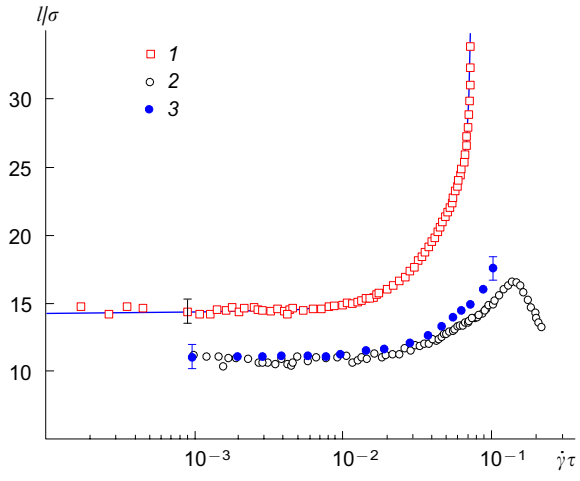


Figure 5. Plots of slip length *vs.* shear rate for atomically flat wall (*1*), for corrugated wall with the wave number $2\pi A/L = 0.27$ (*2*) and for the solution of the Navier – Stokes equation for the same corrugated wall using the Navier boundary condition and the local shear rate-dependent slip length (*3*).[69]

$$\langle V_w \rangle \propto \left(\frac{A}{L}\right)^{-2} \tag{18}$$

The surface roughness patterns of solid materials can differ from the periodic surface reliefs considered above. Often, actual heights of protrusions and distances between them vary stochastically. Mention should be made of surfaces whose roughness is characterized by self-similar hierarchy of the sizes of protrusions and troughs. Structural characteristics of such surfaces on different length scales almost coincide; this is the case of fractal surfaces. The fractal dimension d_f (see a review [68]) is used as a measure of the roughness of a fractal surface. For smooth fractal surfaces one has $d_f = 2$ *vs.* $2 < d_f < 3$ for rough ones. An MD simulation showed that the effective slip length of fractal surfaces exponentially decreases with increasing amplitude of protrusions.[74] This conclusion was qualitatively confirmed by experiments.[29, 30, 67]

Studies [75, 76] on flow over model surfaces patterned with evenly spaced parallel grooves of depth A, width w_g and period L showed that at $A > L$, the longitudinal effective slip length $l_{W,||}$ of simple Newtonian fluid depends on the dimensionless parameter $w = w_g/L$ (see Ref. 76):

$$\frac{2\,l_{W,||}}{L} = \frac{(1-w)\ln(1-w) + (1+w)\ln(1+w)}{\pi} \tag{19}$$

Here the subscript 'W' denotes the Wenzel regime, or homogeneous wetting of the surface of the solid substrate. The dependences of $2l_{W,||}/L$ on the relative depth of grooves at different w values are shown in Fig. 6. As can be seen, the effective slip length considerably increases with increasing the groove width.

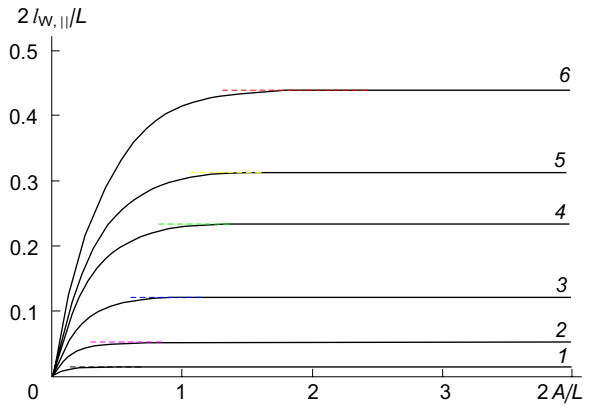


Figure 6. Longitudinal slip coefficient plotted *vs.* groove depth at different dimensionless width w: $w = 0.2$ (*1*), 0.4 (*2*), 0.6 (*3*), 0.84 (*4*), 0.9 (*5*) and 1.0 (*6*).[76]
Dashed lines denote the results of calculations using expression (19).

In contrast to hydrophobic surfaces, rough relief of hydrophilic surfaces can lead to a decrease in the hydrodynamic drag. In particular, this manifests itself in a decrease in the hydrodynamic force as a microsphere approaches the solid substrate. As the height of asperities, A, increases, the effective slip length of aqueous saccharose solutions on a totally wettable surface increases appreciably.[27, 66] Such a paradoxical conclusion was drawn pro-

vided that the distance h between the approaching solid surfaces was measured relative to the virtual boundaries at the tips of asperities. However, in this case one ignores the fact that on a hydrophilic rough surface the virtual boundary corresponding to zero fluid velocity actually lies between the highest and lowest points of the relief. This was proved in relation to a wall with a sinusoidal profile,[77] where the zero velocity level is somewhat higher than the average level and is specified by the normal coordinate

$$y_{\max} = \frac{A^2 K(h/L)}{2h} \tag{20}$$

For the function $K(h/L)$, one has $K(h/L) = 4\pi h/L$ at $h \gg L$ and $K(h/L) \approx 3$ at $h \ll L$. For this case, the apparent slip length defined as

$$l^* = A - y_{\max} \tag{21}$$

was measured in Ref. 66.

Subsequent experiments and results of numerical simulation confirmed the validity of this approach, as applied to randomly rough solid substrates.[78–81] In particular, it was shown that the results of measurements of hydrodynamic drainage force of a water film squeezed from the gap between rough hydrophilic surfaces are well described by expression (11) with the factor f^* equal to[78]

$$f^* = \frac{h}{h + r_s} \tag{22}$$

where r_s is the distance from the average height of the tips of asperities to the virtual level at which the flow velocity is zero. Numerical simulations of displacement of viscous fluids from gaps between approaching sphere and rough hydrophilic surface with randomly distributed protrusions of equal height led to similar conclusion.[79–81] It was established that the hydrodynamic thickness of the liquid film depends on the height A and on the fraction of the surface covered by roughness elements φ_s. As φ_s increases, the distance r_s from the tips of protrusions approaches zero and the hydrodynamic force approaches the value typical of smooth hydrophilic surfaces.

Shear flow of concentrated polymer solutions along rough surfaces is accompanied by a number of interesting features. Studies of the flow of polystyrene (PS) solutions in diethyl phthalate (DEP) between rotating stainless steel disks with a root-mean-square roughness amplitude $A \approx 110$ nm showed that the apparent slip length is a nonmonotonic function of shear stress and can be as large as 140 μm at a polystyrene volume fraction ϕ_{PS} of 8% (Fig. 7 *a*).[82,83] At low measurement accuracy ($\sim$3.5 μm),[83] the slip lengths in a wide range of shear stresses much exceeded the experimental error; therefore, the results obtained can be treated as reliable.

In the case of molecularly smooth surfaces ($A \approx 9$ nm) the slip length also depends nonmonotonically on shear stress. However, an increase in the mean roughness amplitude leads to a marked decrease in the maximum slip length values (Fig. 7 *b*).[83] This was explained by the change in the slip mechanism from the formation of a polymer-depleted layer as a result of the decrease in the configurational entropy of polymer chains near the solid wall with the roughness amplitude smaller than the root-mean-square

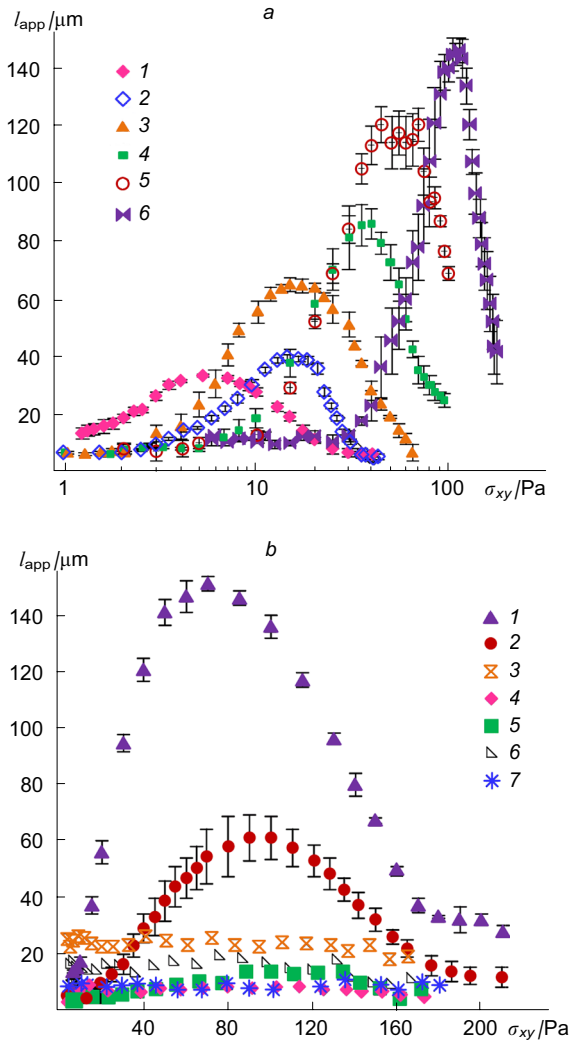


Figure 7. Slip length of PS–DEP solutions plotted *vs.* shear stress at different volume fraction of polystyrene (*a*) and at $\phi_{PS} = 6\%$ and different surface roughness values (*b*).[83]
(*a*) $\phi_{PS} = 2.5$ (*1*), 3 (*2*), 4 (*3*), 5 (*4*), 6 (*5*), 8% (*6*); measurements were carried out on a steel surface with a mean roughness amplitude A of about 110 nm;
(*b*) $A \approx 110$ (*1*), 9 (*2*), 1.4×10^4 (*3*), 657 (*4*), 168 (*5*), 8.5×10^3 (*6*) and 1554 nm (*7*).

radius of polymer coils to disentanglement of polymer molecules at the effective interface between the moving polymer solution and that part of the solution that is localized between roughness elements on the solid surface.[83]

A wall slip mechanism that differs from cohesive slip due to disentanglement of moving polymer chains and surface-adsorbed macromolecules was also considered. The difference consists in the increase in the mobility of polymer chains near the effective interface as compared to adsorbed macromolecules. This makes the early disentanglement of polymer chains less probable and thus favours an increase in the critical stress slip σ_s. Shortening of the slip length with increasing shear stress was associated with non-Newtonian reduction of viscosity of the polymer solution.[83] However, this explanation ignores the possibility of shear-flow-induced formation of wall nano- and microbubbles, as was shown taking a polybutadiene melt as an example.[55] Such

bubbles can be localized in troughs of a rough surface, which leads to inhomogeneous boundary conditions, from sticking to solid areas to slip at fluid/gas interfaces. In the text below we will show that this inhomogeneity of boundary conditions can also lead to a nonmonotonic dependence of the apparent slip length of pseudoplastic fluids on the shear rate.

2.4. Superhydrophobic surfaces

As mentioned above, in the case of homogeneous wetting of a hydrophobic surface (Wenzel state [84]) the surface roughness precludes slip of homogeneous low- and high-molecular-mass fluids and concentrated dispersions and emulsions. Physically, this is due to perturbations of the flow velocity field near microscopic roughness elements.[72, 85] At the same time, localization of gas bubbles in troughs between micropillars can lead to enhancement of slip effects. This is the so-called Cassie – Baxter state [86] and corresponding surfaces are termed superhydrophobic owing to very low wettability. Indeed, the Young wetting angle θ_Y is at most 120° for a flat chemically homogeneous hydrophobic surface, while it usually exceeds a value of 150° and can even approach 180° for superhydrophobic coatings; this favours a ready rolling of droplets.[87] This property is typical of various biological objejcts (Lotus and cabbage leaves, flower petals, grass, butterfly wings, bodies of insects) and artificial superhydrophobic coatings (Fig. 8).[88 – 97]

The wetting angle of a superhydrophobic surface in the Cassie – Baxter state (θ_{CB}) is given by [86]

$$\cos\theta_{CB} = r_f(1-\varphi)\cos\theta_Y - \varphi \qquad (23)$$

Thus the θ_{CB} value depends on the fraction of the fluid/gas interfaces φ, on the surface roughness r_f determined by the ratio of the true contact area to the nominal surface area, and on the Young wetting angle θ_Y of a smooth surface of the material.[84, 98 – 100] In the limiting case $\varphi = 0$ one gets the Wenzel equation [84]

$$\cos\theta_W = r_f\cos\theta_Y \qquad (24)$$

which specifies the wetting angle θ_W of a rough surface in the absence of gas.

At $\varphi \to 1$, for the wetting angle one has $\theta_{CB} \to 180°$. This is the case for surfaces with multi-scale structures including fractal ones.[87, 101 – 103] Note that the expressions for the wetting angles surface in the Cassie – Baxter and Wenzel

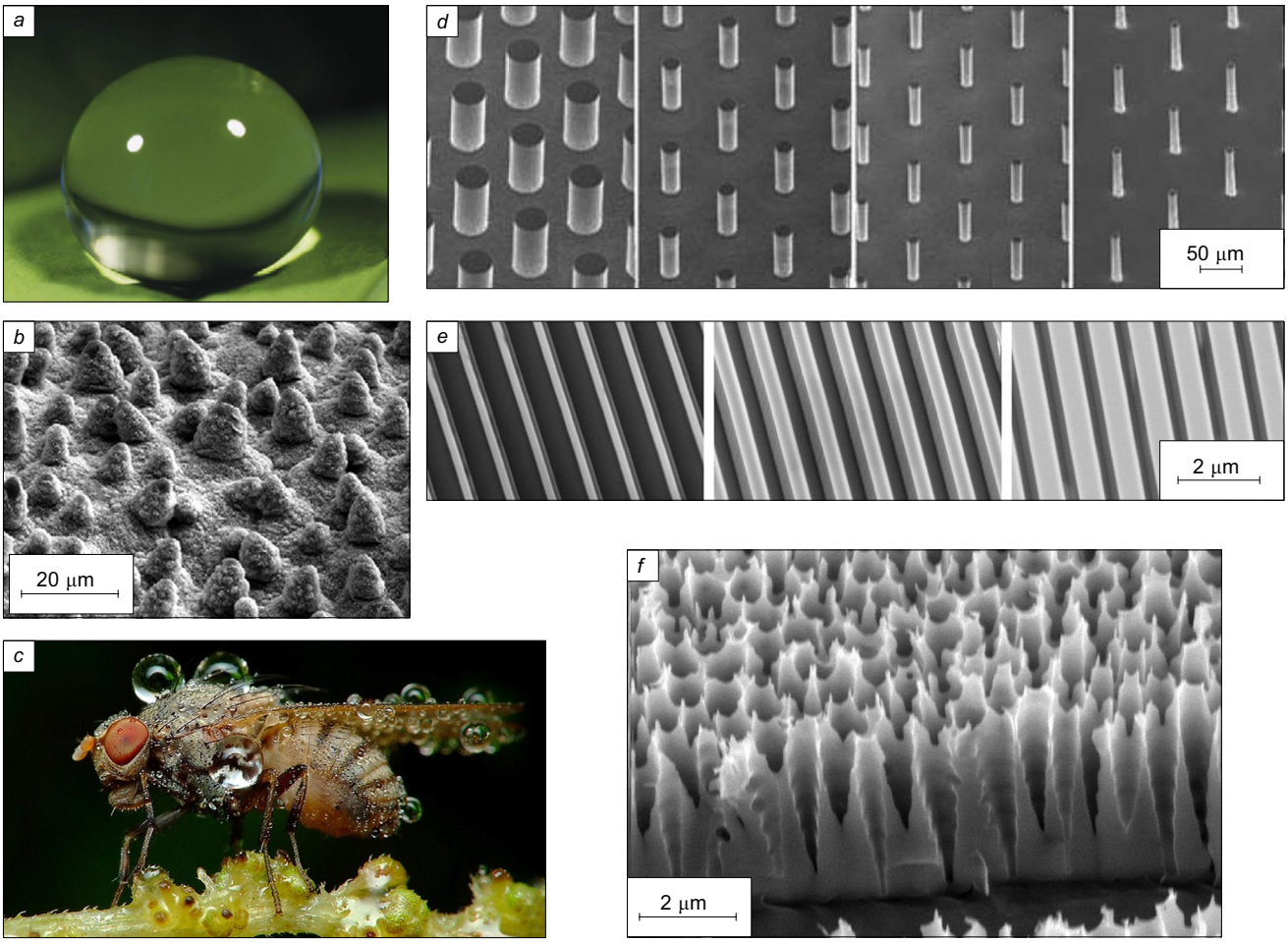


Figure 8. Water droplet on a lotus leaf (*a*) and the surface microstructure of the lotus leaf (*b*);[95] a photograph of a sleeping insect covered in dew (*c*);[88] scanning electron microscopy images of post patterns (*d*),[96] stripe textures with different surface fraction of grooves (*e*),[97] and spiked surface of polyacrylamide (PAA) (*f*).[102]

states are only valid for droplets whose size much exceeds the roughness amplitude.[104]

Alternation of solid microscopic protrusions and gas-filled grooves fundamentally changes the hydrodynamic properties of hydrophobic surfaces owing to alternation of the local boundary no-slip conditions in the fluid–solid contact zones and slip conditions at the fluid/gas interface. As a result, such surfaces are more slippery than smooth hydrophobic surfaces. The effective slip length l_{eff} of simple fluids is given by the ratio of the average slip velocity $\langle V_{\text{w}} \rangle$ to the average shear rate $\langle \dot{\gamma}_{\text{w}} \rangle$ at the wall[77, 105]

$$l_{\text{eff}} = \frac{\langle V_{\text{w}} \rangle}{\langle \dot{\gamma}_{\text{w}} \rangle} \tag{25}$$

$$\langle \dot{\gamma}_{\text{w}} \rangle = \left\langle \left(\frac{\mathrm{d}u}{\mathrm{d}y} \right)_{\text{w}} \right\rangle \tag{25a}$$

(u is the horizontal component of the velocity vector and y is the normal coordinate to the superhydrophobic surface). Expression (25) is valid for isotropically distributed roughness elements. For anisotropic stripe textures (see Fig. 8 *e*) the slip length is different along different directions.[97] To take account of this fact, the effective slip length tensor was introduced[106–108]

$$\mathbf{l}_{\text{eff}} = \langle V_{\text{w}} \rangle \left(\mathbf{n} \langle (\nabla \mathbf{u})_{\text{w}} \rangle \right)^{-1} \tag{26}$$

where $\mathbf{n}$ is the unit normal vector. The effective slip length along ($l_{\text{eff},||}$) and transverse ($l_{\text{eff},\perp}$) to the stripe texture are the eigenvalues of the tensor $\mathbf{l}_{\text{eff}}$. Clearly, one has $l_{\text{eff},||} > l_{\text{eff},\perp}$. In particular, it was shown[109, 110] that for ideal slip at the fluid/gas interface ($l^- \to \infty$) and the no-slip condition at solid protrusions ($l^+ = 0$) one gets the following:

$$l_{\text{eff},\perp} = \frac{L}{2\pi} \ln \left[\cos^{-1} \left(\frac{\pi(1-\varphi)}{2} \right) \right] \tag{27}$$

$$l_{\text{eff},||} = 2\, l_{\text{eff},\perp} \tag{27a}$$

where L is the period of the stripe texture and φ is the surface fraction of gas-filled areas. Relation (27) is valid for a channel whose height h or radius R is much larger than L. Interestingly, expression (27a) holds for arbitrary local slip lengths l^- and l^+.[111] It should also be noted that for Newtonian fluids the effective slip lengths $l_{\text{eff},||}$ and $l_{\text{eff},\perp}$ are independent of the fluid viscosity. From formula (27) it follows that an increase in the fraction of grooves φ causes a rapid increase in the effective slip length along an arbitrary direction. However, near-unity φ values are difficult to reach owing to instability of the Cassie–Baxter state (see below).

Seemingly, the slip length can be increased appreciably on fractal superhydrophobic surfaces with low fraction of the solid phase. However, a theoretical analysis in relation to 2D structures with the fractal dimension $d_{\text{f}} < 2$ showed that this is not the case. Here, the effective slip length obeys the following scaling relationship:[12]

$$l_{\text{eff}} = \frac{3}{8} L \left[\frac{4}{\pi} (1-\varphi) \right]^{(1-d_{\text{f}})/(2-d_{\text{f}})} \tag{28}$$

from which it follows that at specified fraction of solid areas, fractal superhydrophobic surfaces are less effective than superhydrophobic surfaces with regularly patterned roughness. Moreover, at a prescribed wetting angle θ_{CB} the effective slip length on fractal superhydrophobic surfaces decreases with increasing fractal dimension d_{f}. It follows that, unlike smooth hydrophobic surfaces, the effective slip length of 2D fractal superhydrophobic textures is not directly related to the wetting angle.[112]

It should be noted that the slip velocity and slip length on superhydrophobic surfaces can depend on the microchannel thickness h if, *e.g.*, h is comparable with or less than the period L of the stripe texture (Fig. 9).[113–115] However, in a sufficiently wide channel at $h > L$, the effective longitudinal ($l_{\text{eff},||}$) and transverse ($l_{\text{eff},\perp}$) slip lengths depend only on the surface fraction of grooves φ and on the local slip length l on the surface of the grooves. Interestingly, at weak local slip (*i.e.*, at $l \ll L$) over gas-filled areas, the hydrodynamic anisotropy of stripe textures decreases and the longitudinal slip length becomes almost equal to the transverse slip length, that is, $l_{\text{eff},||}/l_{\text{eff},\perp} \to 1$. At the same time, at $l > L$, the effective longitudinal-to-transverse slip length

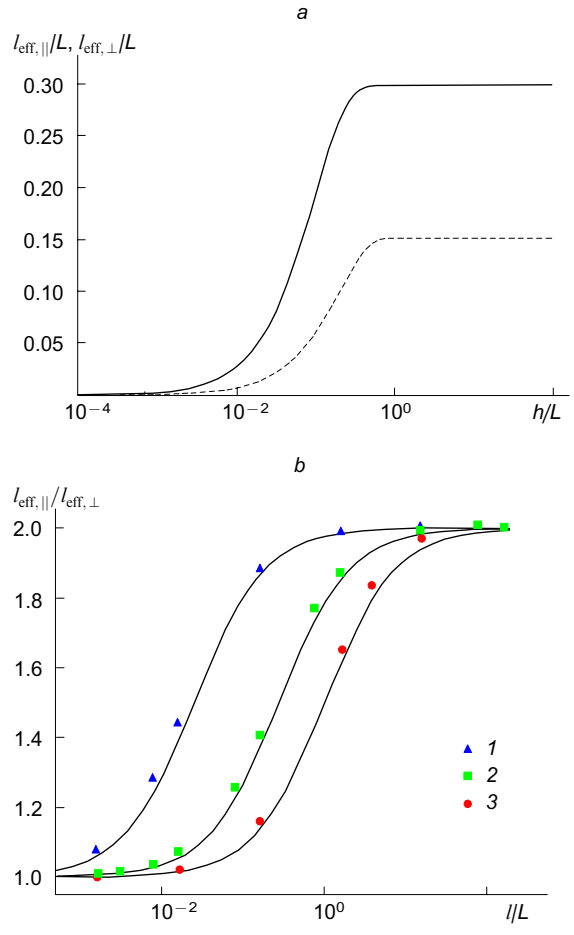


Figure 9. Effective longitudinal $l_{\text{eff},||}$ (solid line) and transverse $l_{\text{eff},\perp}$ (dashed line) slip length of a Newtonian fluid plotted *vs.* relative channel thickness (*a*) and the $l_{\text{eff},||}/l_{\text{eff},\perp}$ ratio plotted *vs.* local slip length at fluid/gas contact areas of a superhydrophobic stripe texture in a wide channel at different φ values (*b*).
(*a*) $\varphi = 0.75$, $l/L = 20$ (see Ref. 115);
(*b*) $\varphi = 0.05$ (*1*), 0.5 (*2*) and 0.95 (*3*).[114]

ratio of a stripe texture is consistent with the known result $l_{\text{eff},\parallel}/l_{\text{eff},\perp} \approx 2$ [see expression (27a)].[109, 110]

Note that the fluid flow on superhydrophobic surfaces is accompanied by perturbations of the velocity field. Having defined such perturbations as

$$\mathbf{u}'(x, y) = \mathbf{u}(x, y) - \langle \mathbf{u}(y) \rangle, \quad (29),$$

where ($\langle \mathbf{u}(y) \rangle$ is the average velocity profile in a channel with the effective slip length $l_{\text{eff},\perp}$), and assuming a flow transverse to the stripe texture, one can show that the perturbations form oppositely directed symmetrical vortices (Fig. 10 *a*).[116] The velocity perturbations are localized near the superhydrophobic wall in a rather wide channel ($h/L > 1$) and propagate to fill the entire cross-section of a narrow channel ($h/L < 1$) (Fig. 10 *b*). As can be seen, the perturbations are much weaker than the velocity U of the upper wall of the channel and of course cannot significantly enhance the convective flow. More efficient mixing is achieved for inclined orientation of the stripe texture which causes the formation of helical flow.[116–118] However, this issue is beyond the scope of this review.

The results discussed above were obtained in the approximation of flat boundary of the fluid/gas contact zones. This approximation works at small fluid pressure difference $\Delta P = P_{\text{ch}} - P_{\text{g}}$ between the channel (P_{ch}) and the gas-filled grooves (P_{g}). The fluid meniscus depth can be estimated [119] as

$$\delta^* = \varepsilon^* g(h, \varphi) L \quad (30)$$

where

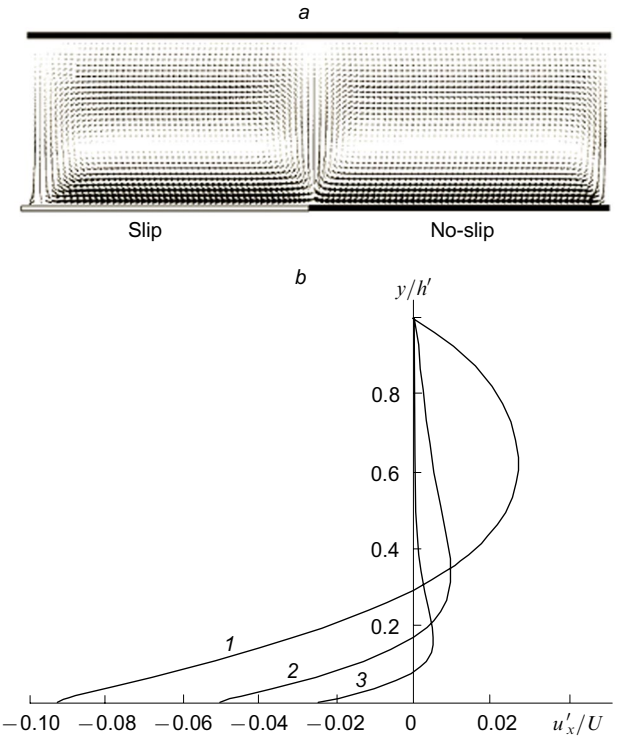


Figure 10. Vector field of flow velocity perturbations $\mathbf{u}'(x, y)$ at $h/L = 0.1$ (*a*) and the change in the horizontal component of the flow velocity perturbations u'_x/U at different channel height at $h/L = 0.5$ (*1*), 0.75 (*2*) and 2 (*3*) (*b*).[116]

$$\varepsilon^* = \frac{L\Delta P}{4\pi\gamma} \quad (30a)$$

In particular, under conditions of the experiment [120] for a wide channel $h \propto L$ at $\varphi = 0.5$, the function $g(h, \varphi) \approx 0.4$ and the meniscus depth is in the range $\delta^* \approx (0.012 - 0.024)L$. In this case the fluid/gas interface can be treated with high accuracy as a flat surface.

However, this is not a versatile case since various scenarios of changes in the shape of the fluid/gas interface are possible. For instance, an increase in the pressure P_{ch} in the channel (or a decrease in P_{g}) can cause the meniscus to sag into the groove, thus leading to instability of the Cassie – Baxter state and to transition to the Wenzel state corresponding to complete wetting.[121, 122] In addition, an increase in P_{g} in grooves (of a decrease in P_{ch}) will favour protrusion of gas bubbles towards the channel [123, 124] and, as a consequence, lead to weakening of slip effects. The search for methods to hold gas bubbles on submerged rough surfaces is of great practical value for reducing the hydrodynamic drag of fluids in microchannels and maintaining effective wall slip.[124–127] In this respect superhydrophobic stripe textures demonstrating a marked decrease in the hydrodynamic drag at relatively high shear rates (~ 11 m s^{-1}) proved themselves.[126]

2.5. Stability of superhydrophobic surfaces

The stability of the Cassie – Baxter state is first of all determined by the degree of hydrophobicity and by the surface roughness pattern of the solid wall.[93, 94] A criterion for thermodynamic stability has the form of inequality for the Young wetting angle, $\theta_{\text{Y}} > \theta_{\text{c}}$, where the critical wetting angle θ_{c} is determined from the expression [128]

$$\cos\theta_{\text{c}} = -\varphi(r_{\text{f}} - 1 + \varphi)^{-1} \quad (31)$$

Clearly, one has

$$0 \leqslant \theta_{\text{c}} \leqslant \frac{\pi}{2} \quad (31a)$$

These inequalities are determined by the value of the roughness parameter r_{f}, which varies from zero for smooth surface to infinity for microporous surface.

In addition to the thermodynamic approach, one should take into account the balance of forces related to hydrostatic pressure difference between the channel and the gas-filled regions (ΔP), as well as the shape of protrusions (see reviews [129–131]). Taking superhydrophobic surfaces covered with periodically patterned micropillars as examples, it was established that the Cassie – Baxter state becomes unstable at

$$\Delta P \geqslant p_{\text{c}} = -\frac{2\gamma(1 - \varphi)\cos\theta_{\text{Y}}}{\varphi r} \quad (32)$$

(here r is the radius of the circular section of microprotrusions).[132, 133] From this criterion it follows that local stability of the fluid/gas interface can be improved by reducing the cross-sectional dimension of protrusions and the distance between them.[132–134] Experiments showed that the critical impalement pressure p_{c} also depends on the protrusion height A. Indeed, the plot in Fig. 11 demonstrates that at $A < 20$ μm, the critical pressure linearly increases and

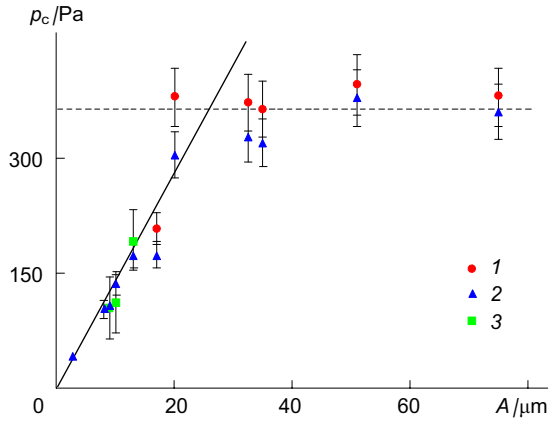


Figure 11. Critical impalement pressure plotted *vs.* height of micropillars.[133]
Experiments: evaporation (*1*), compression (*2*) and drop impact (*3*). Dashed line is the best fit of experimental data at $h > 20$ μm.

reaches a plateau at $A > 20$ μm.[133] This behaviour of p_c was explained by the fact that at small height of micropillars one has $\cos\theta_Y \approx A$, whereas at relatively large A values, the wetting angle θ_Y has time to reach its maximum value corresponding to the critical inflow wetting angle at which the contact line spontaneously slips along the microprotrusion.[133] In addition, in the case of superhydrophobic stripe textures, the critical pressure increases as the width-to-depth ratio of the gas-filled grooves increases.[135]

At pressures higher than p_c, transition from the Cassie–Baxter state to the Wenzel state occurs by gradual sagging the fluid meniscus into troughs (Fig. 12 *a*).[121] The critical time of complete wetting t_c exponentially decreases with increasing pressure ΔP (Fig. 12 *b*).

In addition, the lifetime of a thin gas layer above the superhydrophobic surface immersed in water exponentially decreases as the hydrostatic pressure increases.[136] This phenomenon was explained using the Henry law, according to which an increase in hydrostatic pressure causes an increase in the concentration of dissolved gas and an

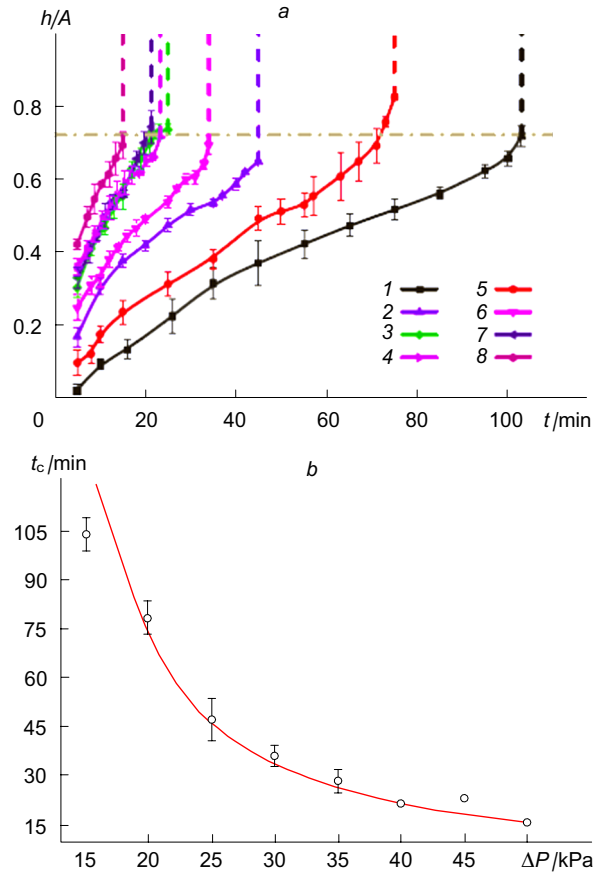


Figure 12. Relative sagging depth of the meniscus plotted *vs.* time at different fluid pressures (*a*) and the critical collapse time of the meniscus plotted *vs.* applied pressure ΔP (*b*).[121]
(*a*) ΔP = 15 (*1*), 20 (*2*), 25 (*3*), 30 (*4*), 35 (*5*), 40 (*6*), 45 (*7*), 50 kPa (*8*).

exponential increase in the partial pressure of the gas in the fluid. This idea was further developed [122,123] and it was shown that pressure-driven fluid flow over superhydrophobic wall can lead to acceleration of gas exchange between

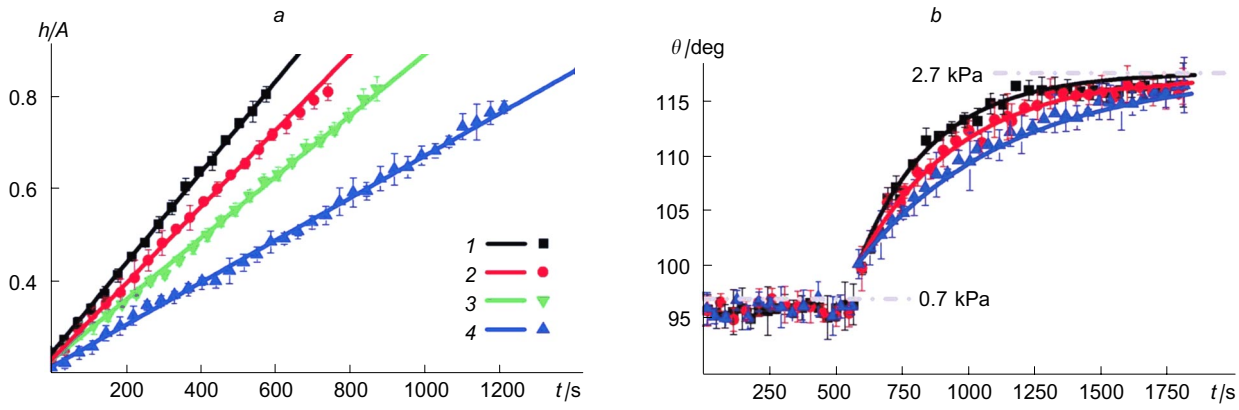


Figure 13. Relative sagging depth of the meniscus h/A in the metastable state plotted *vs.* time at a pressure ΔP of 11.7 kPa and different Reynolds numbers (Re) (*a*) and the change in the wetting angle θ in the pinned Cassie–Baxter state plotted *vs.* time due to a pressure drop from ΔP = 0.7 to 2.7 kPa; t = 600 s (*b*).[122]
Re = 16.68 (*1*), 8.34 (*2*), 4.17 (*3*), 2.08 (*4*).

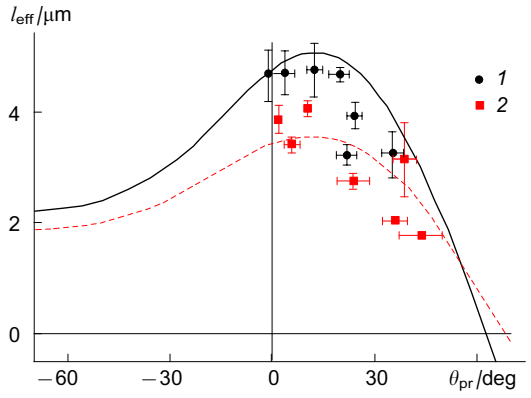


Figure 14. Transverse effective slip length plotted *vs.* protrusion angle θ_{pr} at two values of the fraction of the surface covered with bubbles: $\varphi = 0.38$ [dashed line is drawn using the results of calculations, solid circles (*1*) denote experimental data] and $\varphi = 0.54$ [solid curve is drawn using the results of calculations, solid squares (*2*) denote experimental data].[141]

gas-filled cavities and bulk fluid. A confocal microscopy study [122] showed that, similarly to hydrostatic pressure, the flow can cause a gradual sagging of meniscus and thus trigger the wetting transition (Fig. 13 *a*). The fluid pressure in the channel was maintained to acquire the pinned Cassie – Baxter state, or, contrary to this, depinned states.[122, 137] Sagging of meniscus into troughs of the superhydrophobic surface in the pinned Cassie – Baxter state is accompanied by changes in the wetting angle (Fig. 13 *b*). Shear flow had almost no effect on the equilibrium states of meniscus in the studied range of Reynolds numbers.[122]

When the pressure in the gas bubbles exceeds the fluid pressure, gas bubbles protrude from troughs. In this case the efficiency of slip of a simple fluid depends on the protrusion angle of gas bubbles (θ_{pr}). An increase in this angle towards the liquid layer ($\theta_{pr} > 0$) initially leads to some increase in the effective slip length l_{eff} compared to flat fluid/gas interface and then to a marked decrease in l_{eff}.[138 – 143] This behaviour was qualitatively confirmed in various experiments [124, 141, 144] (see Fig. 14). Slip vanishes at the critical protrusion angle θ_c; at $\theta_{pr} > \theta_c$, the effective slip length becomes negative, thus indicating that the mattress of convex bubbles causes an increase in friction.

Theoretical and numerical estimates showed that for different types of roughness including transversely arranged roughness elements, $\theta_c \approx 65°$.[140, 141] It should be noted that fluid flow in a channel with superhydrophobic stripe texture is characterized by an increase in the effective slip length with increasing protrusion angle up to 90°.[145, 146]

2.6. Specific features of slip of non-Newtonian fluids in channels with superhydrophobic wall

The aforesaid concerned effective slip of simple Newtonian fluids. The nature of slip of non-Newtonian polymer fluids along superhydrophobic walls has been poorly studied so far. The authors of numerical and theoretical studies [144, 147, 148] on the regularities of slip of non-Newtonian pseudoplastic media considered aqueous solutions of xanthan gum [144] and PAA;[147] the viscosities of these systems depend on the shear rate $\dot{\gamma}$ and are well described by the Carreau – Yasuda model

$$\eta(\dot{\gamma}) = \eta_\infty + (\eta_0 - \eta_\infty)\left[1 + (\lambda\dot{\gamma})^a\right]^{(n-1)/a} \quad (33)$$

where η_0 and η_∞ are the limiting viscosities at zero and infinitely high shear rate, respectively; the parameter λ specifies the width of the Newtonian plateau, the exponent n is the slope of the viscosity curve; and the parameter a characterizes the sharpness of transition from Newtonian plateau to non-Newtonian behaviour.

For calculations of Poiseuille flow in a round channel and Couette flow between parallel plates transverse to the superhydrophobic texture, it was shown that the extrapolation slip length l_{app} is a nonmonotonic function of the longitudinal pressure gradient dp/dx (Fig. 15 *a*) [144] and the basic shear rate $\dot{\gamma}$ (Fig. 15 *b*).[147] This result was confirmed qualitatively in a theoretical study.[148] The plots in Fig. 15 demonstrate that the maximum extrapolation slip length noticeably increases with increasing exponent n which characterizes the rate of change in the viscosity specified by the Carreau – Yasuda equation (33), *viz.*, the steeper the viscosity curve the longer the slip length. Figure 15 *a* dem-

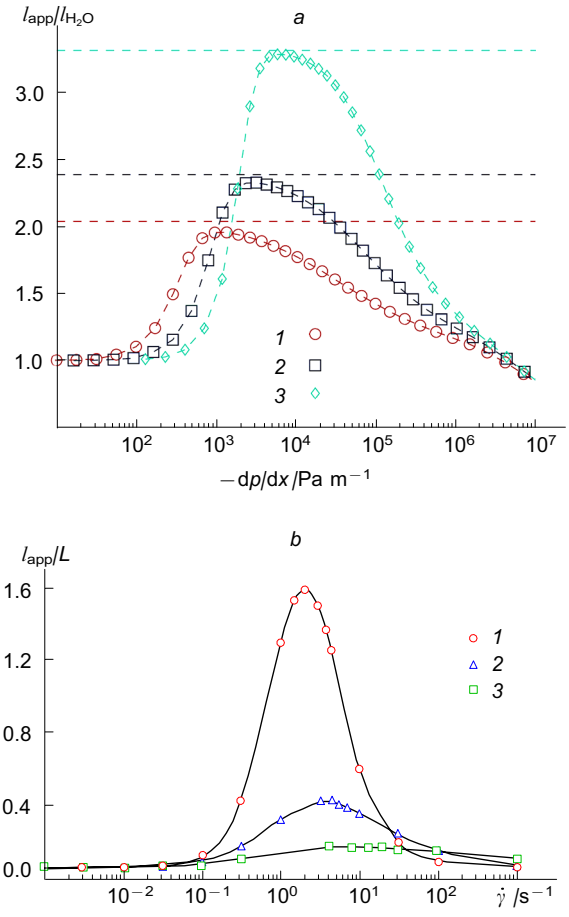


Figure 15. Apparent slip length plotted *vs.* pressure gradient dp/dx for Poiseuille flow and cylindrical geometry of channel (*a*) [144] and *vs.* basic shear rate $\dot{\gamma}$ for Couette flow transverse to superhydrophobic texture with the surface fraction of grooves $\varphi = 0.5$ (*b*).[147] (*a*) $n = 0.563$, $c = 0.05$ mass % (*1*); $n = 0.503$, $c = 0.10$ mass % (*2*); and $n = 0.406$, $c = 0.20$ mass % (*3*);
(*b*) $n = 0.1$ (*1*), 0.2 (*2*) and 0.4 (*3*).

onstrates a similar behaviour of the ratio of l_{app} to the effective slip length of pure water (l_{H_2O}) at the n values lying in a narrower range $0.406 < n < 0.563$ corresponding to the change in the xanthan gum concentration (c) from 0.05 mass % to 0.20 mass %.[144] In both cases, the fraction, φ, of the fluid/gas contact areas is $\varphi = 0.5$.

The physical mechanism of slip of a pseudoplastic fluid along a superhydrophobic wall is as follows.[147] Figure 16 *a* shows that near the superhydrophobic wall the mean velocity profiles of the flow of aqueous PAA solution along and transverse to the stripe texture become nonlinear, whereas the velocity profiles of Newtonian fluids remain linear. It follows that, unlike the slip of Newtonian fluids, that of pseudoplastic media is apparent. The effect originates from the viscosity perturbations near the superhydrophobic wall (Fig. 16) due to local perturbations of the shear rate.[147] In the vicinity of the solid areas with the no-slip boundary condition, the fluid slows down. This causes an abrupt decrease in viscosity, whereas at the fluid/gas interface the shear rate is zero and the viscosity of pseudoplastic fluid approaches η_0 [see expression (33)]. As a result, an inhomogeneous near-wall layer is formed. The effective viscosity of this layer is lower than the bulk fluid viscosity.

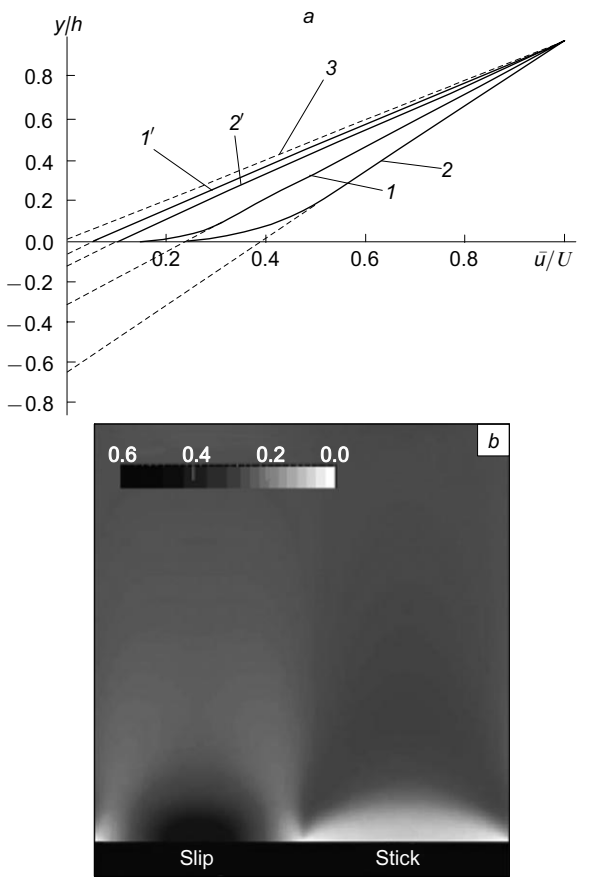


Figure 16. Mean velocity profiles of a Newtonian fluid (*1′*, *2′*) and pseudoplastic aqueous PAA solution (*1*, *2*) across (*1′*, *1*) and along (*2′*, *2*) superhydrophobic stripe texture with the fraction of grooves $\varphi = 0.5$ in a channel with the thickness h; (*3*) velocity profile in a channel with smooth solid walls ($\varphi = 0$) under the basic shear rate $\dot{\gamma} = 1\ s^{-1}$ (*a*) and the relative viscosity field $\eta(x,y)/\eta_0$ of aqueous PAA solution under simple shear flow across the superhydrophobic stripe texture at $h/L = 1$ (*b*).[147]

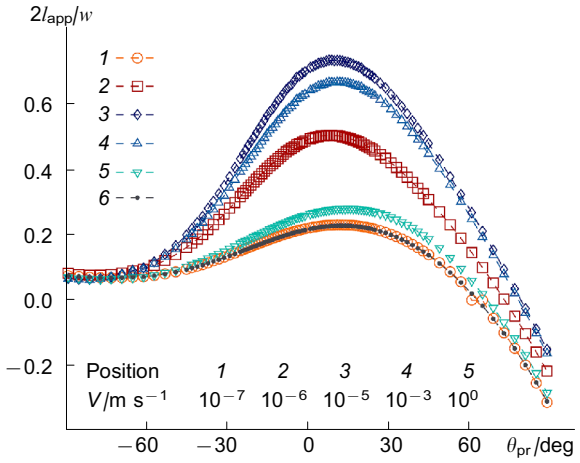


Figure 17. Relative apparent slip length $2l_{app}/w$ for the flow of 0.2% xanthan gum aqueous solutions (*1–5*) and water (*6*) across a superhydrophobic texture plotted *vs.* protrusion angle θ_{pr} at different mean Poiseuille flow velocities ($h = 100$ μm, $\varphi = 0.5$, grooves 10 μm wide).[144]

The apparent slip lengths, both along and transverse to the stripe texture, are much larger than the corresponding effective slip lengths of Newtonian fluids. Thus, the use of pseudoplastic media will allow one to significantly decrease the hydrodynamic drag of microchannels.

In conclusion, mention may be made of an interesting result.[144] For an aqueous xanthan gum solution, it was shown that the protrusion of gas bubbles in the case of flow of a pseudoplastic medium in a round capillary causes an additional increase in the apparent slip length compared to the situation in pure solvent (see Fig. 17).[144] The slip length is a specific function of the shear rate, which is due to viscosity variations of the pseudoplastic medium in the vicinity of gas bubbles (see above).

In summary of this Chapter, factors influencing characteristics of the slip of homogeneous low- and high-molecular-mass fluids demonstrate the variety of slip mechanisms that should be taken into account in the analysis of experimental data, design of microdevices and when posing and solving fundamental problems related to the interaction of fluids with channel walls made of different materials and having different surface structures.

3. Interaction of multicomponent fluids with solid wall

3.1. Structural features of multicomponent fluids

The flow of multicomponent colloidal and polymeric systems of complex architecture (concentrated microgel emulsions and suspensions, colloidal solutions of star polymers, melts of block copolymers with micellar structure, suspensions of dendrimers, solid particles coated with a layer of grafted macromolecules, multilayer capsules, *etc.*) is characterized by nontrivial features of the interaction with solid walls. For instance, disperse systems behave as viscoplastic materials with pronounced yield stress if the volume fraction of particles (ϕ) is of the order of or higher than the critical value ϕ_g corresponding to the glassy state. Such media can flow only at stresses σ that exceed the yield stress σ_y, while at $\sigma < \sigma_y$ they exhibit the properties of sol-

ids.[149, 150] According to a classification system,[151] a glassy state of suspensions of noninteracting monodisperse solid spheres is achieved at ϕ_g values in the range $0.58 < \phi_g < 0.64$. Microgel suspensions undergo a glass transition at higher concentrations, namely, at $0.64 < \phi_g < 1$; the fraction of the disperse phase in emulsions with close-packed droplets can be as high as 0.96.[152 – 154] High concentration of close-packed star polymers is due to specific features of macromolecular interpenetration, while highly concentrated (compressed) emulsions are prepared by transforming spherical droplets to hexagonal ones; this is accompanied by dramatic decrease in the fraction of the free interparticle space (Fig. 18 *a*).[152] The rheological properties of such systems allow them to be treated as viscoplastic media.[152, 153] Wall slip of highly concentrated dispersions and emulsions enables considerabe reduction of the energy loss during the flow in microchannels, which is of great practical interest.

At relatively low content of the disperse phase ($\phi < \phi_g$) the presence or absence of wall slip of suspensions depends on the character of the interaction between micro- or nanoparticles. Wall slip of suspensions of stabilized (repelling) solid particles is only possible is the binder slips. However, the slip velocity of low-molecular-mass fluids on hydrophobic or lyophobic surfaces is very low since in this case the slip length is a few tens of nanometres.[4, 7, 10] If a high-molecular-mass binder is used as a continuum medium, the hydrodynamic behaviour of suspensions will be determined by the laws of wall slip of polymer melts. Besides, colloidal gels prepared from attracting particles usually demonstrate wall slip.[154 – 159]

Consider specific features of the flow of highly concentrated suspensions of soft particles (microgels, capsules, liposomes, block copolymer micelles, latex particles and solid particles coated with grafted polymer layers) and concentrated emulsions. When close packed, particles in the concentrated emulsions undergo deformation and adopt the shape of compressed polyhedra.[152, 160 – 162] A model system comprising soft elastic spheres with the volume fraction $\phi = 0.8$ is shown in Fig. 18 *b*.[163] Close packing of colloidal particles eliminates the temperature factor, and the rheological response of concentrated dispersions is mainly due to overcoming of geometric constraints imposed on particles by their nearest neighbours. Removing constraints depends strongly on the balance between forces of pair elastic interparticle interactions and external stresses. Mac-

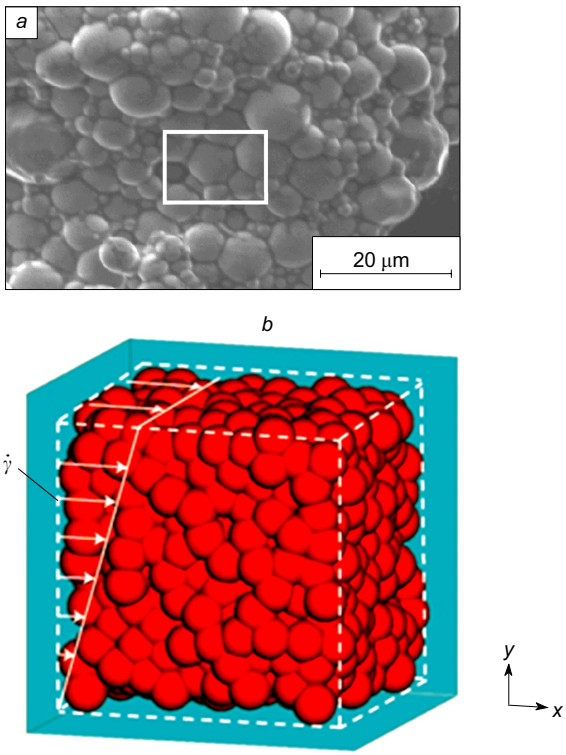


Figure 18. Photomicrograph (*a*) and a schematic (*b*) of highly concentrated emulsions containing deformed droplets that adopted polyhedral shape.
(*a*) Well-defined polyhedra are clearly seen;[152]
(*b*) typical configuration of an array of compressed elastic spheres at $\phi = 0.8$.[163]

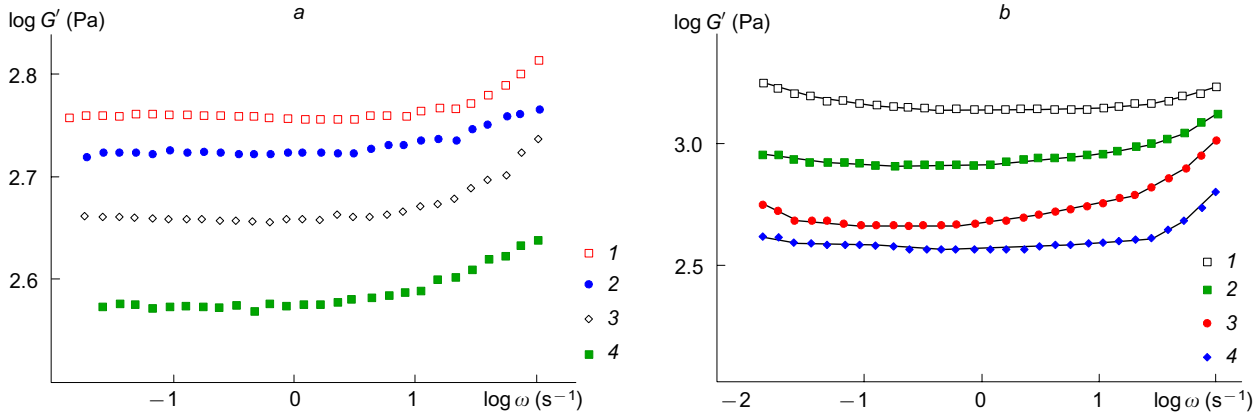


Figure 19. Frequency dependences of the elastic modulus of water-in-oil emulsions (*a*) and emulsions containing droplets of different size at constant concentration of the aqueous phase of 91% [see *Colloid J.*, **69**, 185 (2007)].
(*a*) Emulsions with aqueous phase concentrations of 95 (*1*), 94 (*2*), 93 (*3*), 92% (*4*);
(*b*) emulsions with droplet sizes of 8.2 (*1*), 11 (*2*), 14 (*3*) and 20.5 mm (*4*) at constant concentration of the aqueous phase.

roscopic motion of such dispersions near solid surfaces depends on the chemical nature and on the degree of roughness of channel walls.

At shear stresses lower than the yield stress, the systems in question behave as elastic solids.[164] Like that of solids, their elastic modulus (G') is is independent of frequency (ω) in the linear region of viscoelastic response, *i.e.*, at low stresses and small deformations (Fig. 19).

Depending on the nature of soft polymer particles, their elastic properties are determined by different physical mechanisms. For instance, elastic response of neutral star polymers, microgels and concentrated emulsions is due to the osmotic pressure of polymers in solvents and to entropy losses associated with stretching of polymer chains,[165–167] and to interparticle interactions.[152, 168] Contrary to this, rigidity of polyelectrolyte microgels depends on the osmotic pressure of counterions,[169] while the elastic properties of liposomes and capsules are governed by the compression and flexural moduli of the surrounding membranes.[170] Here, it is appropriate to mention a new class of droplets called 'liquid marbles'. The surface of 'liquid marble' droplets is covered with a layer of solid microparticles;[171–175] their Young modulus depends on the interfacial tension, on the equilibrium wetting angle of the liquid phase as well as on the size and surface density of solid microparticles.[173]

It is convenient to characterize the elasticity of soft particles by the dimensionless parameter

$$\psi = \frac{G_p R^3}{kT} \tag{34}$$

where G_p and R are respectively the elastic modulus and the hydrodynamic radius of particles.[151, 176, 177] The parameter ψ varies in a rather wide range depending on the solvent quality and on the molecular architecture of colloidal particles. One has $\psi \approx 1$ for macromolecular coils, $\psi \approx 10^3$ for star polymers ($f \approx 100$ arms), $\psi \approx 10^4$ for microgels and $\psi \approx 10^6$ for nanoemulsions, capsules and liposomes.[151] Unlike star polymers and micelles whose elastic potentials depend only on the number of stars

$$\psi \approx f^{3/2} \tag{35}$$

the elasticity of microgels, droplets and microcapsules depends on their radius. The corresponding dependences are as follows:[178, 179]

$$\psi \approx \frac{R^3}{v_0 N} \tag{36a}$$

$$\psi \approx \frac{\gamma R^2}{kT} \tag{36b}$$

$$\psi \approx \sqrt{BK} R^2 \tag{36c}$$

where v_0 and N are the volume and number of statistical chain segments between microgel cross-link points, γ is the interfacial tension, and B and K are the compression and bending moduli of microcapsule membranes. The parameter ψ of non-Brownian particles can take rather large values.

3.2. Wall slip and yield stress

With all the variety of concentrated suspensions and emulsions, their rheological behaviour is characterized by a number of common features (see reviews [18, 151, 152, 179–181]). In particular, typical shear flow curves of concentrated emulsions [179, 182–185] shown in Fig. 20 are qualitatively consistent with corresponding flow curves of concentrated suspensions of solid particles,[186–190] and soft microgels [191–197] and concentrated solutions of star polymers [198] and colloidal gels.[156, 159] As can be seen, the flow curves depend crucially on the degree of wall roughness. In particular, flow of concentrated dispersions between two rough walls is possible only if the shear stress exceeds a certain critical values, that is, the yield stress σ_y. An increase in the shear rate is accompanied by nonlinear increase in stress. This rheological behaviour is usually well described by the Herschel–Bulkley equation [199]

$$\sigma = \sigma_y + k\dot{\gamma}^m \tag{37}$$

where $\dot{\gamma}$ is the true shear rate of the dispersion and the exponent m is close to 0.5 for almost all concentrated dispersions mentioned above.[155, 163, 187, 191, 192, 200] At stresses higher than the yield stress ($\sigma > \sigma_y$), the flow of concentrated dispersions occurs by local structural rearrangements driven by certain particles that succeed to remove constraints associated with close packing (cage effect). These processes originate from the competition between long-range plastic deformations and local elastic interparticle interactions.[200, 201]

These regularities are also observed in channels with smooth walls at rather high shear stresses.[191–194, 198] However, if the stress is lower than the yield stress ($\sigma < \sigma_y$), the flow curves of concentrated dispersions exhibit a kink instead of a plateau with a constant shear stress; subsequent decrease in the shear rate is accompanied by a decrease in the stress (see Fig. 20).[186, 191–194, 198, 199, 202] This is also observed in measuring the first difference of normal stresses N_1 during slow shear flow. Normal stresses are independent of the apparent shear rate since they are determined by

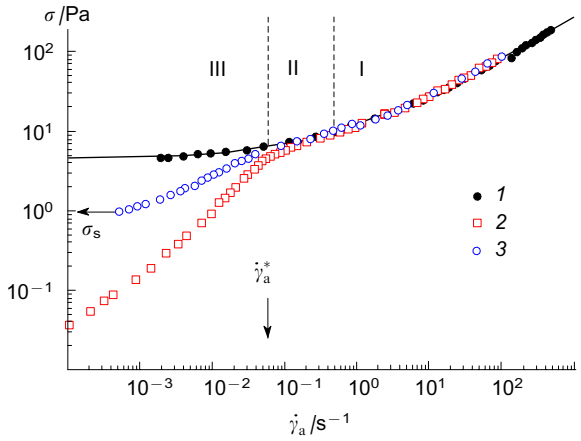


Figure 20. Flow curves for a concentrated emulsion sheared between two rough surfaces (*1*) and between a rough surface and a smooth hydrophilic (*2*) and hydrophobic (*3*) surface. The solid curve is a fit to the Herschel–Bulkley equation (37); $\dot{\gamma}_a^*$ is the apparent shear rate at $\sigma = \sigma_y$; and σ_s is the sticking yield stress.[179] I–III are different flow regimes (see text).

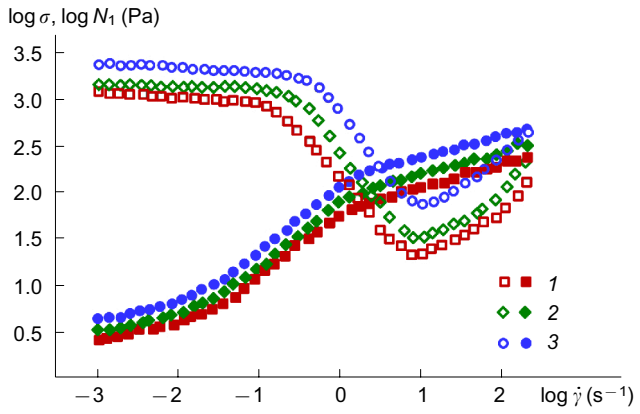


Figure 21. Plots of the first difference of normal stresses N_1 (open symbols) and shear stresses σ (solid symbols) *vs.* shear rate for concentrated emulsions at different volume fractions of the dispersed phase: 92 (*1*), 93 (*2*) and 94% (*3*).[203]

Reynolds dilatancy and abruptly decrease as flow begins (Fig. 21).[203] This behaviour of normal stresses is a direct consequence of wall slip at low shear stresses. Interestingly, the inflection point in the dependence of $\log N_1$ on $\log\dot{\gamma}$ corresponds to the yield stress σ_y.

As wall slip arises in the gap between solid surfaces moving in opposite directions at the velocity U, the true shear rate of the medium, $\dot{\gamma}$, becomes smaller than the apparent shear rate, $\dot{\gamma}_{app} = 2U/h$, and is defined as

$$\dot{\gamma} = \dot{\gamma}_{app} - \frac{\chi V_w}{h} \qquad (38)$$

where V_w is the wall slip velocity, h is the width of the gap between the plates and the coefficent $\chi = 1$ or 2 for one or two smooth surfaces, respectively. This was clearly demonstrated by direct measurements of shear rate profiles.[182, 187, 191 – 193, 204 – 210]

3.3. Shear banding and wall slip

The velocity profiles of complex fluids can exhibit local kinks (Fig. 22 *a*),[211] thus indicating instability of deformation processes of complex fluids, which are accompanied by the appearance of zones of intense shear deformations called shear bands or strain localization.[17, 152, 205 – 207] Typical flow curves of colloidal dispersions and solutions of worm-like micelles can include negative-slope portions corresponding to unstable flow regimes; in this case one deals with shear rate-dependent stress (see Fig. 22).[208 – 212]

Instability of shear flow of concentrated suspensions can manifest itself in discontinuities of the structure of the medium, *i.e.*, inhomogeneous motion of layers (Fig. 23).[210] The presence of different-type structures in multicomponent materials owing to bifurcation of their properties (in the form of coexistence of two structural states) was observed in various complex fluids including colloidal dispersions and emulsions,[17, 159, 187, 205, 213 – 215] micellar [209, 216 – 218] and polymer solutions.[219 – 222] The effect can be smoothed out by a broad molecular mass distribution (MMD) of polymers. In this connection one may talk of continuous nonlinear profile of simple shear rates instead of a shear rate drop.[223]

A deep interrelation between wall slip and shear banding should be emphasized.[207, 224 – 227] For instance, studies of concentrated polymer solutions revealed that wall slip usually precedes the formation of flow inhomogeneities under the action of external shear stresses since adhesion

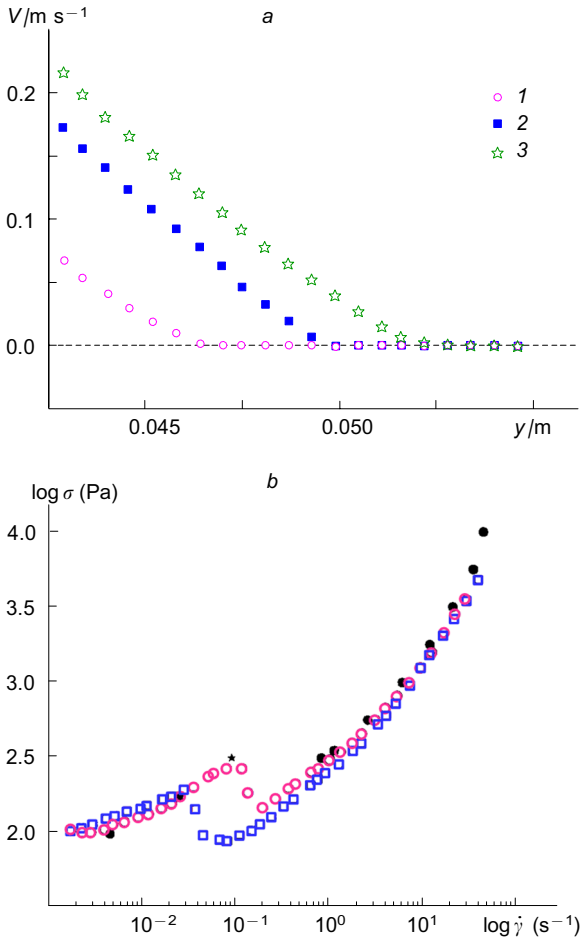


Figure 22. Velocity profiles for a cement paste at different rotation rates of the walls of a Couette instrument (*a*)[211] and shear stress curves for a monodisperse suspension with the volume fraction, ϕ, of PS $\phi = 0.45$ under shear banding (*b*).[212]
(*a*) Velocities were assessed by magnetic resonance velocimetry; rotation rate of the walls of the Couette instrument /rpm: 30 (*1*), 60 (*2*) and 70 (*3*).

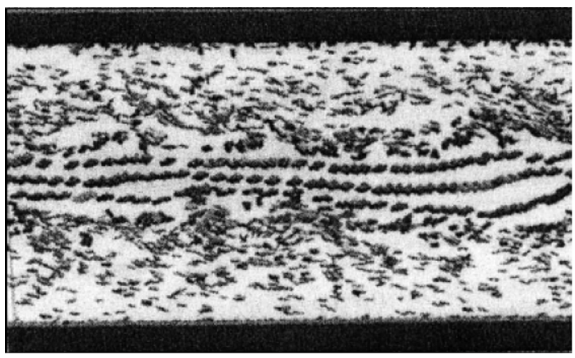


Figure 23. Discontinuations appeared under simple shear flow of granulated materials.[210]
The distance between the lower and upper plates is $h = 1.8$ mm.

to the solid wall is usually weaker than cohesive strength.[208, 224–227] Shear bands were observed in, *e.g.*, channels with smooth walls when the Weissenberg number (Wi) exceeded the critical value

$$\mathrm{Wi} > \mathrm{Wi_c} = 1 + \frac{2\,l_{\max}}{h} \tag{39}$$

where $l_{\max}$ and h are the maximum slip length and the width of the gap, respectively. Figure 24 *a* presents the velocity profiles of concentrated polybutadiene solution at effective shear rates of 0.3 and 3 s^{-1}, which corresponds to Wi = 20 and 200, respectively.[224] The critical Weissenberg number of this polymer solution is $\mathrm{Wi_c} = 26$. This provides an explanation for the fact that at $\mathrm{Wi} < \mathrm{Wi_c}$, one deals with almost plug flow with predominantly wall slip, whereas at $\mathrm{Wi} > \mathrm{Wi_c}$, the velocity profile exhibits a sharp local kink accompanied by a decrease in V_w.[224] Similar changes were also observed in a study on the flow of concentrated aqueous suspensions of microgel particles in a channel with hydrophobic surface (Fig. 24 *b*), namely, an increase in the slip velocity V_w relative to the bulk velocity U leads to the appearance of a kink in the velocity profile and to extension of the region where fluidization of the medium occurs.[226]

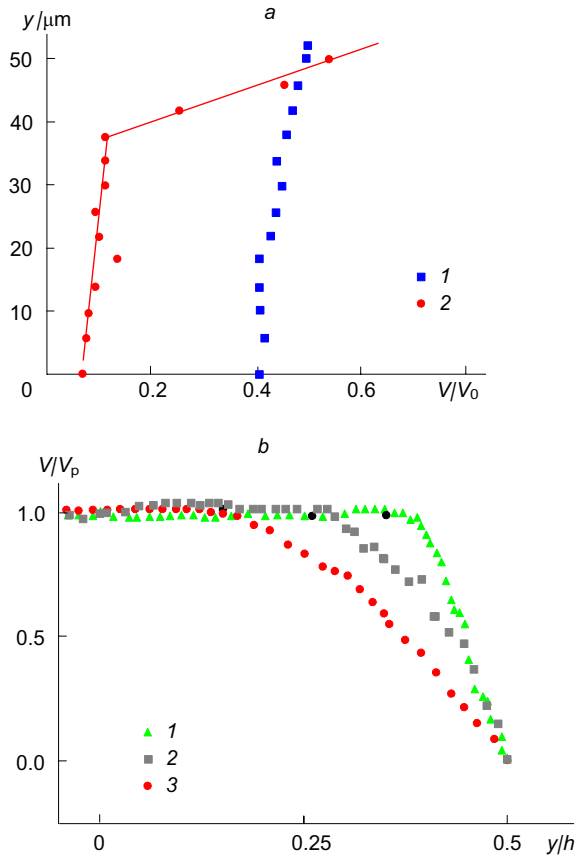


Figure 24. Velocimetrically assessed steady-state velocity profiles of particles of 13% polybutadiene solution (M_w = 1000 kg mol^{-1}) in microchannels 50 μm wide at an average effective shear rate of 0.3 (*1*) and 3.0 s^{-1} (*2*) (*a*)[224] and concentrated apparent suspensions at different relative wall slip velocities (*b*).[226]
(*b*) $V_w/U = 0.5 \times 10^{-2}$ (*1*), 8.5×10^{-2} (*2*), 10^{-1} (*3*). V_p is the central plug velocity in the plug flow profile.

3.4. Wall slip and the properties of channel walls

To understand the physical nature of wall slip of disperse fluids, it is critically important to directly measure corresponding flow velocity profiles along rough and smooth solid walls. The results of flow velocity measurements for a concentrated microgel suspension (hydrodynamic particle radius 220 nm) at different shear stresses are shown in Fig. 25.[191] The measurements were carried out at a fixed distance from the axis of rotation of a cone–plate rheometer with rough and smooth walls. One can see that at stresses below the yield stress σ_y, a linear velocity profile is formed between rough walls prepared by sticking sand paper on the shearing surfaces and no wall slip or shear bands are observed.

Contrary to this, wall slip between smooth walls coated with a polymer film does occur. A decrease in shear stress leads to an increase in the slip velocity V_w relative to the linear velocity of the cone at a specified distance from the axis of rotation and to a decrease in the true velocity gradient of the suspension. If the stress is lower than the yield stress ($\sigma < \sigma_y$), the slip velocity becomes equal to the wall velocity; the velocity profile corresponds to plug flow and the true shear rate is zero (see Fig. 25 *d*).[191] In this case, the suspension moves like a solid only due to wall slip. This corresponds to regime III in the rheological curves (see Fig. 20).[179] If the shear stress much exceeds the yield stress (see Fig. 25 *b*), wall slip can be ignored (see regime I in Fig. 20). The true shear rate differs only slightly from the apparent shear rate ($\dot\gamma_{app} \approx \dot\gamma$). In this regime the flow curve of the dispersion matches the flow curve between rough surfaces. Direct flow velocity profile measurements showed that in a narrow stress range near the yield stress $\sigma_y \leqslant \sigma \leqslant 1.5\,\sigma_y$, the flow of concentrated suspensions and emulsions is also accompanied by wall slip (see regime II in Fig. 20).[179, 191, 192] In this case the appearance of a kink in the flow curve complicates a correct determination of the yield stress. Seemingly, it is regime II (see Fig. 20) that is associated with the region of sharp decrease in normal stresses (see Fig. 21).[203]

The character of wall slip depends on the nature of interparticle interaction (attraction or repulsion) and on the affinity of the wall material and the binder (hydrophilicity or hydrophobicity).[156–158, 167] It was established that in all cases the slip velocity of a concentrated suspension of soft polymer particles below the yield stress is a power function of the stress applied[182, 191–193, 204]

$$V_w \approx V_y(\sigma - \sigma_s)^k \tag{40}$$

where V_y is the slip velocity at the yield stress $\sigma = \sigma_y$ and σ_s is the slip threshold (stress below which no wall slip is observed). The coefficient k is unity for hydrophobic surfaces and repelling colloidal particles[194, 204] and $k \approx 2$ for hydrophobic surfaces and attracting particles.[156–158] Dependence (40) was confirmed experimentally (see Fig. 26).[179]

In Fig. 26 one can see that the slip threshold σ_s of microgel pastes on hydrophilic surfaces is much lower than that on hydrophobic ones.[179] In the former case the low slip threshold can be explained by the fact that at the wall, microgels are separated from the hydrophilic surface by a

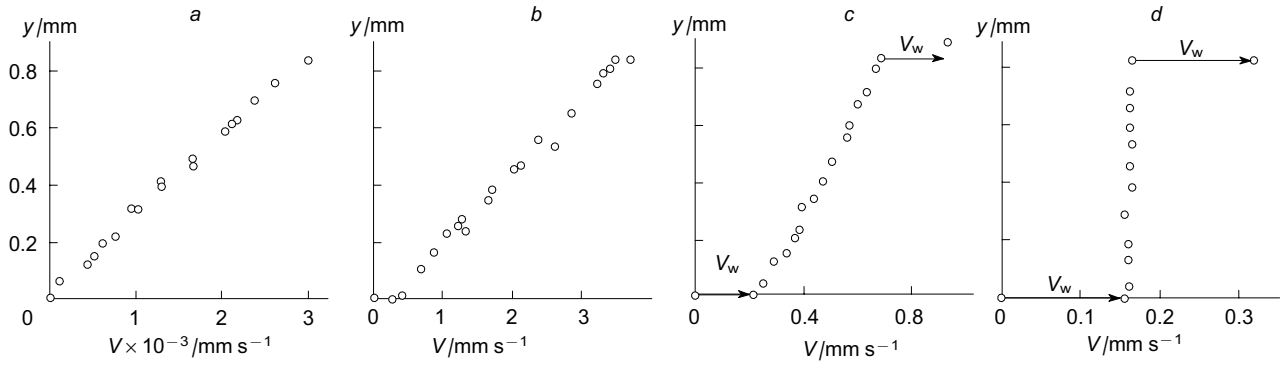


Figure 25. Velocity profiles for a microgel suspension under shear flow between rough surfaces at $\sigma/\sigma_y = 1.05 \pm 0.1$ (*a*) and between smooth surfaces at $\sigma/\sigma_y = 1.7 \pm 0.1$ (*b*), 1.3 ± 0.1 (*c*) and 0.9 ± 0.1 (*d*).[191]
$V \times 10^{-3}$ /mm s^{-1}

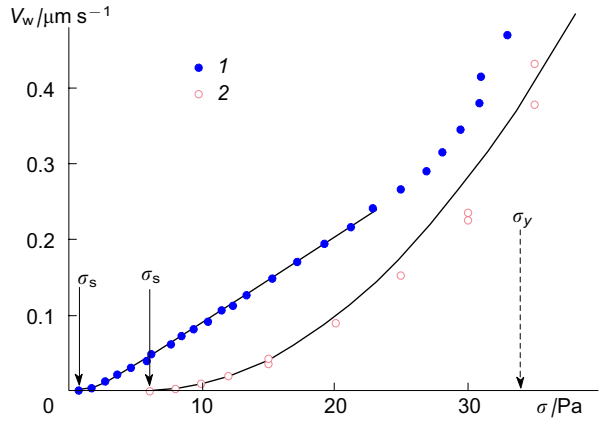


Figure 26. Microgel paste slip velocity plotted *vs.* shear stress on hydrophilic (*1*) and hydrophobic (*2*) surfaces.[179]
The dashed arrow denotes the yield stress $\sigma_y = 34$ Pa, the solid arrows denote the slip thresholds $\sigma_s = 0.7$ and 5.8 Pa for the hydrophilic and hydrophobic surfaces, respectively.

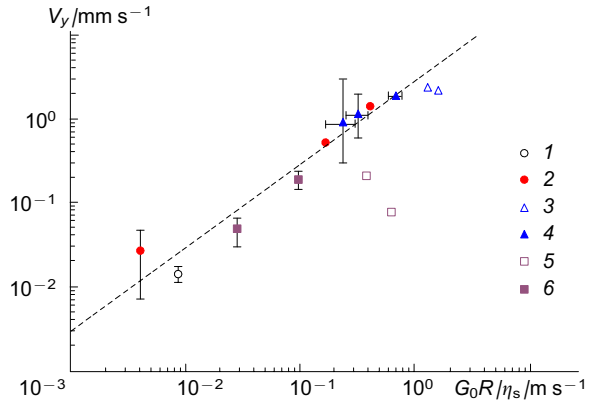


Figure 27. Slip velocity V_y at the yield stress σ_y plotted for concentrated emulsions at different volume fractions of the dispersed phase φ (*3*, *4*) and for microgel pastes (*1*, *2*, *5*, *6*) at different cross-link density N_x, solvent viscosity η_s and polymer concentration C.[191]
Emulsion: $\varphi = 0.86$, 0.93 (*3*), 0.71, 0.75, 0.77 (*4*)

Pastes:

Position	*1*	*2*	*5*	*6*
N_x	140	28	140	140
η_s/mPa s	9	0.9	0.9	0.9
C/g g^{-1}	0.02	0.045, 0.055, 0.065	0.04, 0.06	0.015

thin layer of binder (water), which enables their slip at low shear stresses. Pushing such particles away from the hydrophobic wall requires a low force. In both cases the slip threshold is much lower than the yield stress ($\sigma_s \ll \sigma_y$). An indirect proof of the existence of a low-viscous near-wall fluid layer is provided by the inversely proportional dependence of the slip velocity of the medium, V_y, on the solvent viscosity (η_s) at yield stress. Experimental data on the wall slip velocities obtained for different concentrated microgel and emulsion pastes with different hydrodynamic radii of particles (R), degrees of cross-linking of polymer networks and solvent or binder concentrations and viscosities are well approximated by the following expression (Fig. 27):[191]

$$V_y \approx \frac{G_0 R}{\eta_s} \tag{41}$$

where G_0 is the shear modulus of the dispersion. A similar dependence was observed for apparent slip along a thin layer of thickness δ (see Fig. 1 *b*) [7]

$$V_w \approx \frac{\delta\sigma}{\eta_s} \tag{42}$$

The thickness, δ, of the near-wall layer of a concentrated microgel dispersion can be estimated from the dynamic equilibrium condition for a thin solvent film and a squeezed particle. From the Reynolds equation for a lubricating layer [228] it follows that

$$\delta^2 \approx \eta_s V_w \frac{r_0}{p_0} \tag{43}$$

where r_0 is the radius of the flat face of the deformed particle and p_0 is the pressure in the thin film at the solid wall. On the other hand, from Hertzian contact mechanics one has

$$r_0 \approx R\zeta^{1/2} \tag{44}$$

and the elastic stress of the particle is given by

$$\sigma_p \approx G_p \zeta^{1/2} \quad (45)$$

where G_p and ζ are respectively the elastic and shear moduli of the spherical particle.[229] From the equilibrium condition $\sigma_p = p_0$ it follows that the thickness of the lubricating layer increases with increasing solvent (binder) viscosity, particle radius and wall slip velocity [191]

$$\delta \approx \left(\frac{\eta_s V_w R}{G_p} \right)^{1/2} \quad (46)$$

For hydrogel pastes (220 nm particle radius) this simple expression gives the thickness of the near-wall layer $\delta \approx 2-10$ nm, which is almost independent of the concentration of particles.[192]

Colloidal gels of attracting particles exhibit wall slip at concentrations that are much lower than concentration corresponding to close packing of particles. In particular, slip is observed for flow of weakly flocculated colloidal dispersions of poly(methyl methacrylate-*co*-ethylhexyl methacrylate) [154] and silica particles with grafted poly(butyl methacrylate) chains in a poor solvent.[155] The thickness of the near-wall liquid layer in these colloidal gels agrees in order of magnitude with the data for microgel pastes (see above).

The slip mechanism for concentrated suspensions of solid microparticles is somewhat different. In this case apparent slip is due to a decrease in the filler concentration near the solid wall owing to the steric interaction between particles and channel walls. As a result, the thickness, δ, of the lubricating layer depends on the average size R, the volume fraction ϕ and the limiting degree of packing ϕ_{max} of the solid particles. A simple relationship [188]

$$\delta = 2R\left(1 - \frac{\phi}{\phi_{max}}\right) \quad (47)$$

describes experimental data with a reasonable accuracy; note that $\delta \approx 0.1R$ at $0.46 < \phi < 0.6$.[230–232] In this type of suspensions, roughness of channel walls can induce fracture of the deformed samples instead of preventing slip.[233]

Double S-shaped pattern of the dependence of $\log\eta$ on $\log\sigma$ observed for certain colloidal suspensions of weakly attracting particles and concentrated emulsions can be due to the existence of the slip threshold σ_s.[13, 155, 183, 233–235] As an example Fig. 28 presents these dependences for dispersions based on poly(methyl methacrylate-*co*-ethylhexyl methacrylate) in low-aromatic white spirit that flocculate on adding nonadsorbing polyisobutylene.[154] Measurements carried out under flow between coaxial cylinders with a smooth and a rough inner cylinder showed that in both cases at low shear stress the viscosity of the dispersion is high. In the case of rough walls at $\sigma < \sigma_y$, the viscosity decreases continuously, which corresponds to plastic flow associated with structural breakdown in the bulk. Experiments with cylinders with smooth walls revealed a sharp decrease in viscosity at lower stresses followed by reaching an intermediate plateau. This was followed by further viscosity drops at stresses equal to those observed in the case of rough-wall stresses inducing macroscopic flow of the dispersion. The intermediate plateau viscosity, which is a few orders of magnitude lower than the 'zero' viscosity, reduces as the width h of the gap between the rotating cylinders decreases. This is indicative of wall slip of the dispersion in the stress range studied.[156]

The results presented in Fig. 28 *b* and similar data were obtained by measuring compliance under creep conditions.[155, 156] At low stresses, creep of the dispersion can be due to elastic deformations of gel formed by attracting particles. However, interpreting the results of these measurements in the range of maximum Newtonian viscosity values requires more thorough studies.[152] Similar curves were observed in viscosity measurements of low-density polyethylene (LDPE)/metaboric acid blends using a cone–plate rheometer (Fig. 29).[236]

Thus, wall slip of multicomponent dispersions and colloidal systems arises at particular energy and mechanical interactions. There are two types of wall slip. One arises under shear of viscoplastic media that can exist in two different physical states, a solid (at stresses lower than the yield stress) and a liquid one (at stresses higher than the yield stress). Transition from the solid to liquid state (either sharp or thixotropic) is accompanied by transition from

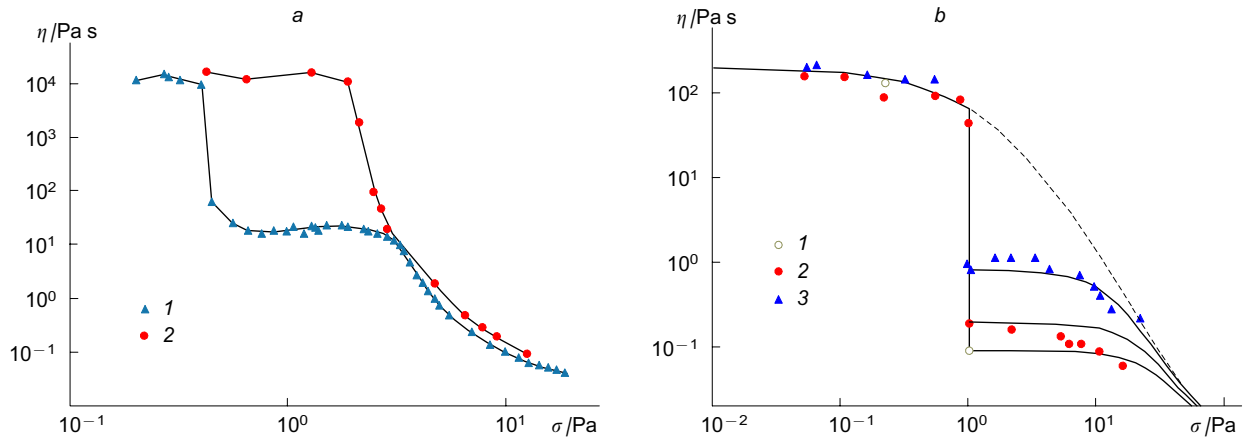


Figure 28. Steady-state viscosity plotted *vs.* shear stress for dispersions of 0.4 mass % poly[(methyl methacrylate)-*co*-(ethylhexyl methacrylate)] in white spirit containing polyisobutylene flowing in channels between coaxial cylinders with smooth (*1*) and roughened (*2*) walls (*a*) and in channels with smooth walls at the channel width h = 0.5 (*1*), 1.07 (*2*) and 5.0 mm (*3*) (*b*).[154]

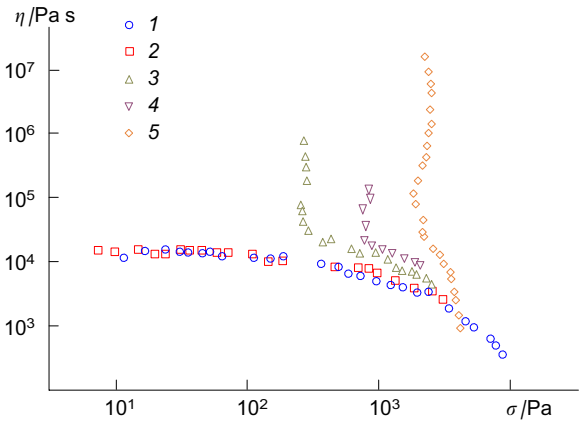


Figure 29. Plots of steady-state viscosity of LDPE/metaboric acid blends *vs.* shear stress at 180 °C.
Volume fraction of metaboric acid: 0.068 (*1*), 0 (*2*), 0.141 (*3*), 0.396 (*4*) and 0.304 (*5*).[236]

wall slip to real flow. The reverse transition from the liquid to solid state occurs in highly concentrated suspensions under high shear rates or under large deformations owing to the glass transition induced by the deformation processes. The other type of slip arises as a result of dynamic formation of a thin low-viscous fluid layer at the channel wall. This leads to drop of the shear rate and looks as apparent slip.

4. Polymer melts

4.1. Physics of slip of polymer melts along solid wall

Polymer melts are a kind of fluids and it is just the possibility of irreversible deformations of these systems that underlies many technological processes of fabrication of polymeric items. Being single-phase and one-component media (unlike the materials discussed in Section 3), polymer melts can slip along solid walls of channels where they flow. Understanding of the mechanism of this phenomenon is of great importance for both physical chemistry of polymers and technological applications. The onset of slip of polymer melts is due to both physics of molecular (relaxation) motions of long-chain polymers and interfacial interactions. It should be noted that the flow – slip transition characterizes the instability of motion and is closely related to self-oscillations of the system.

The flow – slip transition at high deformation rates originates from bifurcation of the rheological properties related to the relaxation nature of polymer deformations. Amorphous polymers demonstrate different types of rheological behaviour depending on the time scale of observation. A typical dependence of the elastic modulus of amorphous polymers G on the deformation frequency ω is shown in Fig. 30.

The occurrence of the transition in question means that elastic deformations become dominant compared to irreversible deformations both under shear and under tension. This pattern of transitions corresponds to the linear region of mechanical behaviour (small deformations). However, the situation remains valid as the deformation rate (or corresponding stress) rather than the deformation frequency (small deformations) increases since acceleration is

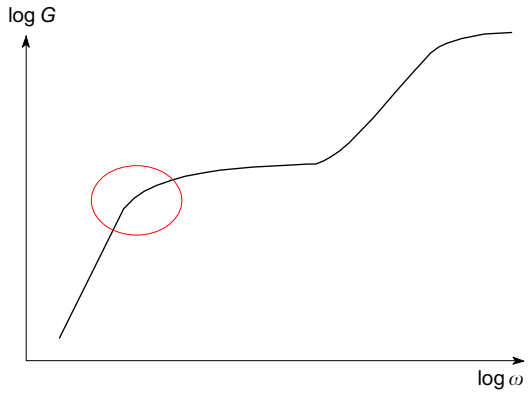


Figure 30. Flow – rubbery transition (ringed) upon increase in deformation frequency.

equivalent to the decrease in the characteristic time of deformation. This transition is schematically depicted in Fig. 31.

Thus, at high stresses (and corresponding high deformation rates) a polymer melt behaves as a solid-like material. When under shear, this leads to slip along a solid surface (*cf.* polymer jet break under tension). The concept of slip onset as a consequence of relaxation transition of the polymer melt was formulated in the pioneering studies of researchers from the scientific school headed by Prof. G.V.Vinogradov,[237–240] who discovered the spurt effect, *i.e.*, a sudden detachment of polymer melt from the solid

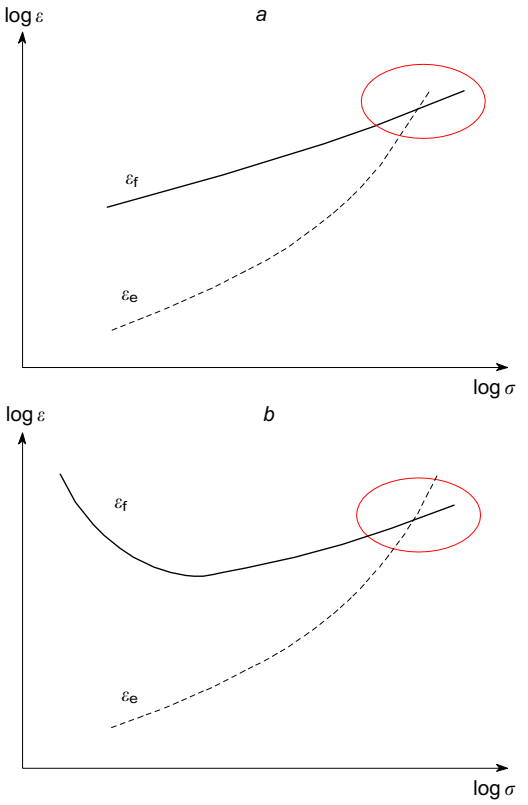


Figure 31. Flow deformations (ε_f) and elastic deformations (ε_e) plotted *vs.* shear stress (*a*) and tensile stress (*b*).
The regions of flow – rubbery transitions are ringed.

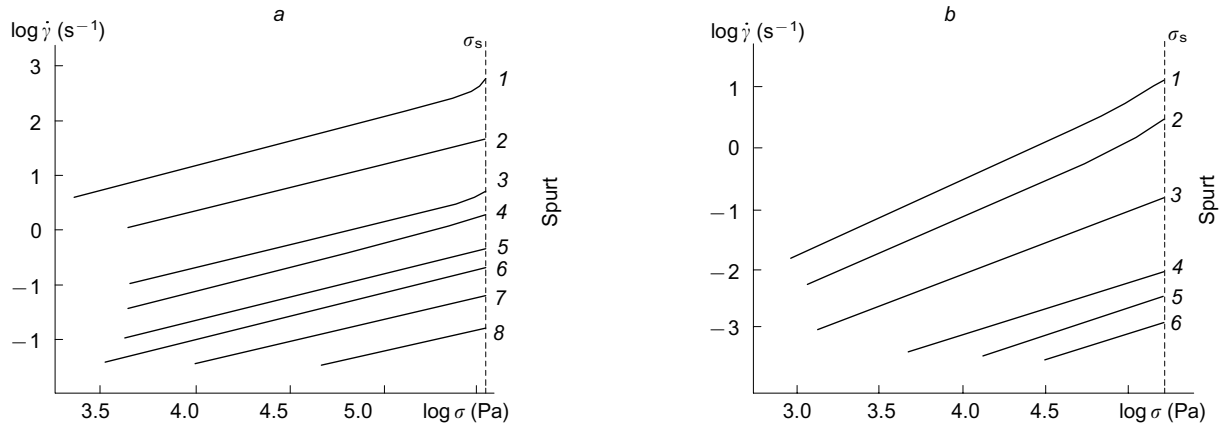


Figure 32. Flow breakdown in flow curves for series of melts of monodisperse polybutadienes (*a*) and polyisoprenes (*b*).[237]
(*a*) Molecular mass (MM) × 10^{-3} = 38 (*1*), 67 (*2*), 102 (*3*), 151 (*4*), 204 (*5*), 240 (*6*), 320 (*7*) and 580 (*8*);
(*b*) MM × 10^{-3} = 106 (*1*), 148 (*2*), 282 (*3*), 355 (*4*), 422 (*5*) and 575 (*6*).

wall accompanied by huge increase in the volumetric flow rate under capillary flow.

This concept was developed [241–246] from the standpoint of intermolecular entanglements. A possible mechanism of the transition in hand was as follows. It was assumed that at high deformation rate, the characteristic time of the process becomes shorter than the characteristic time required for disentanglement to occur. Therefore, as the deformation rate increases, macromolecules have no time to slip into entanglement knots while the entanglement knots do not disentangle. Rather, they are tightened, thus forming a quasi-stable network (on the time scale of experimental shear rates). The spurt for series of polymers having different molecular masses is schematically shown in Fig. 32.[237]

The spurt and flow slip most clearly manifest themselves in the case of flow of monodisperse flexible-chain polymers. As to the flow of industrial polydisperse samples, the spurt effect is smoothed over owing to superposition of relaxation properties of different components in the MMD.

Slip of a dielectric (polymer) on a metallic surface causes electrization of the polymer jet; the electrostatic charge increases with increasing slip velocity.[242–246] This phenomenon is illustrated in Fig. 33.[245] Slip of polymer melts on solid surfaces was observed in many studies (see, *e.g.*, Ref. 247). At present, this phenomenon is basic to rheology of polymers.

An clearly seen condition for the flow–rubbery transition is specified by the critical Weissenberg number

$$\mathrm{Wi}^* = \dot{\gamma}\tau \approx 1 \tag{48}$$

where $\dot{\gamma}$ is the shear rate and τ is the characteristic relaxation time. The following simple rearrangements allow one to relate Wi* to the stress σ_{sp}, at which flow breakdown occurs: since

$$\dot{\gamma} = \frac{\sigma_{sp}}{\eta} \tag{49}$$

and

$$\tau = \frac{\eta}{G} \tag{50}$$

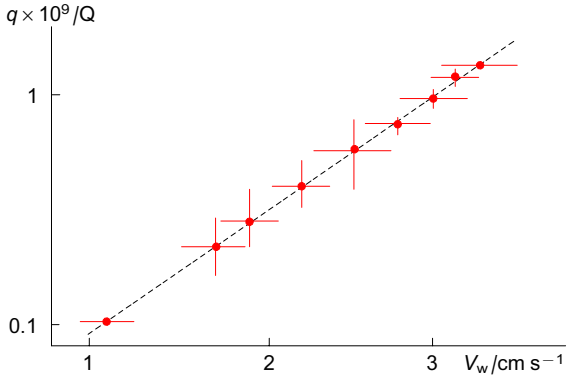


Figure 33. Electrostatic charge (q) of polymer jet plotted *vs.* slip velocity on metallic surface of a capillary.[245]

where G is the elastic modulus and η is viscosity, one gets

$$\mathrm{Wi}^* = \frac{\sigma_{sp}}{G} \tag{51}$$

The elastic modulus of monodisperse polymers is independent of the molecular mass of polymers of a given homologous series and, therefore, spurt, *i.e.*, the onset of slip, occurs at a certain constant stress σ_{sp} = const (see Fig. 32).

The σ_{sp} values reported in different publications can differ from one another since they depend on the method of measurements. For flexible-chain polymers (polyisoprene and polybutadiene) the σ_{sp} values determined in the earlier studies [237–240] and more recently confirmed by other authors are 0.3–0.4 MPa. The σ_{sp} value of polydimethylsiloxane lies in the range from 0.057 to 0.07 MPa.[248] Polyethylene is characterized by appreciably different σ_{sp} values equal to 0.22, 0.1, 0.1 and 0.26 MPa. These differences can be explained by the effect of subtle differences in the polyethylene chain structure on the properties of the polymer.[248–250] A contribution from the roughness of the solid surface cannot also be excluded. For polyisobutylene one has σ_{sp} = 0.09 MPa.[251] Polymers with different chemical

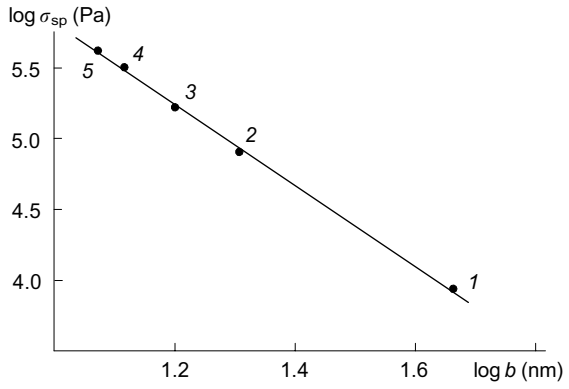


Figure 34. Spurt stress plotted *vs.* Kuhn segment length.[252] Polyphosphazene (*1*), polystyrene (*2*), polyisoprene (*3*), polybutadiene (*4*) and linear polyethylene (*5*).

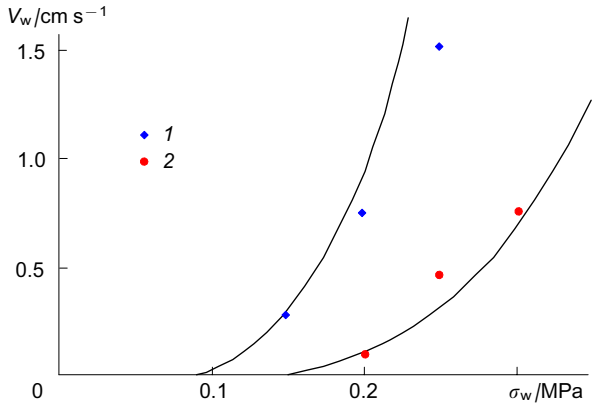


Figure 36. Plots of slip velocity *vs.* shear stress at different MMD patterns.[261]
Molecular mass 5.8×10^4, broad MMD (*1*) and MM = 3.1×10^4, narrow MMD (*2*).

structure, *e.g.*, polyphosphazenes, are characterized by a very small σ_{sp} value of 0.009 MPa.[252] Most likely, in this case the decisive role is played by the polymer chain flexibility. Indeed, a correlation between σ_{sp} and the Kuhn segment b was found (Fig. 34).[252]

Progress in methods for direct observation of velocity profiles in the channel cross-section (velocimetry methods[253 – 264]) made it possible to measure the flow velocity in the immediate vicinity of the solid channel wall with a resolution of at least 30 μm. Using these methods, it was shown that the velocity of flowing polymer melts at the wall can differ from zero, *i.e.*, the classical no-slip hypothesis is in some cases invalid.

Spurt can be to some extent smoothed over on going from monodisperse polymers to mixtures of fractions or to industrial materials.[256] This can be explained using the experimental data presented in Fig. 35 where the flow curves for two monodisperse polymers and their blends are shown. As can be seen, the rheological properties change appreciably on going from monodisperse polymers to blends, *viz.*, an extended region of non-Newtonian flow appears and the shear rate (not shear stress!) corresponding

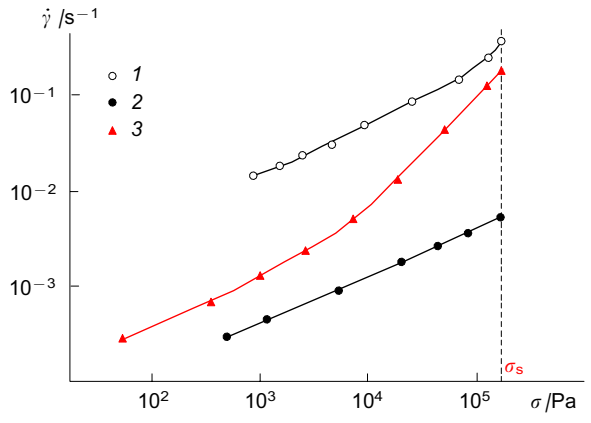


Figure 35. Non-Newtonian spurt – slip region appearing on going from monodisperse polyisoprenes (*1*, *2*) to their blends (*3*).[256]
MM = 3.8×10^4 (*1*), 2.4×10^5 (*2*); and a blend of polymers *1* and *2* in a 0.7 : 0.3 ratio (*3*).

to the onset of slip abruptly increases. Both these effects are due to superposition of the relaxation properties of different fractions in the polydisperse polymer;[257,258] as a consequence, high-molecular-mass fractions undergo transition to the rubbery state, being surrounded by fractions that retain their fluidity.

Thus, the conditions for the flow – slip transition depend strongly on the MMD of the polymer.

The influence of the MMD on the slip onset conditions was demonstrated experimentally.[261 – 263] Indeed, slip can develop gradually in the polymer MMD-dependent stress region (Fig. 36) rather than arise in jumpwise manner (like abrupt flow breakdown), as shown in Fig. 32.

Flow of polydisperse polymers is accompanied by deformation fractionation at which low-molecular-mass fractions undergo diffusion towards high stresses, *i.e.*, towards the solid wall. This leads to formation of a thin, relatively low-viscous layer near the solid surface, which looks as apparent slip. A similar effect is observed in the case of interfacial slip under layer-by-layer flow of different polymers.[259, 260]

4.2. Slip velocity determination according to Mooney

The possibility for polymer melts to slip when forced through capillaries was for the first time considered by Mooney[8] taking rubber compounds as examples. The assumption of slip was made based on the experimental data that demonstrated an abnormal dependence of the volumetric flow rate of the mixture on the capillary diameter. The case in point is that under slip one should add the standard volumetric flow rate Q_{shear} that is determined using the Hagen – Poiseuille equation with a certain excess volumetric flow rate Q_{slip} corresponding to the motion of bulk material with the slip velocity V_w. The observed volumetric flow rate Q is the sum of Q_{shear} and Q_{slip}. For a Newtonian fluid with the viscosity η one has

$$Q = Q_{shear} + Q_{slip} = \frac{\pi D_p^4 \Delta P}{128 \eta L_p} + \frac{\pi D_p^2}{4} V_w \qquad (52)$$

where D_p and L_p are the capillary diameter and length, respectively, and ΔP is the pressure drop along the capillary.

The equation for the shear stress at the capillary wall follows from the law of conservation of momentum and has the form

$$\sigma_w = \frac{\Delta P D_p}{4 L_p} \tag{53}$$

At σ_w = const, one deals with

$$Q = \frac{\pi D_p^3}{64\eta}\sigma_w + \frac{\pi D_p^2}{4} V_w \tag{54}$$

or

$$\frac{64 Q}{\pi D_p^3} = \frac{1}{\eta}\sigma_w + \frac{16}{D_p} V_w \tag{55}$$

This equality underlies the Bagley method for slip velocity calculations. It involves plotting the dependence $\dot{\gamma}_w = 64\,Q/\pi D_p^3$ on D_p^{-1} and its extrapolation to $D_p^{-1} = 0$. The slope of the plot is equal to V_w, while the intersection point of the straight line with the ordinate axis at $D_p^{-1} = 0$ gives the true viscosity value. It should be noted that both measured parameters (V_w and η) characterize a particular shear stress value and can generally depend on it. This traditional method for slip velocity calculations was used by the authors of numerous studies (see, *e.g.*, Refs 251 and 264–266) and is illustrated in Fig. 37.

A similar method for slip velocity measurements was proposed for rotational flow between two parallel disks.[267] In this case, the gap h between disks was varied and the apparent shear rate $\dot{\gamma}_{app}$was measured for two values of this parameter (h_1 and h_2) at different shear stresses σ_w. The formula for calculations has the form

$$V_w(\sigma_w) = \frac{\dot{\gamma}_{app,1}(h_1, \sigma_w) - \dot{\gamma}_{app,2}(h_2, \sigma_w)}{2\,(h_1^{-1} - h_2^{-1})} \tag{56}$$

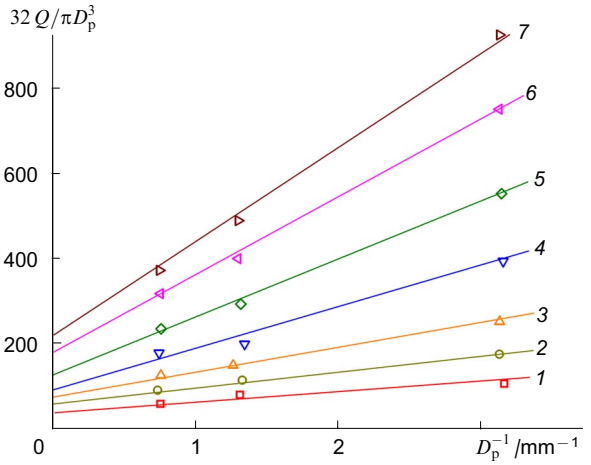


Figure 37. Volumetric flow rate plotted *vs.* capillary diameter at different shear stresses.[251]
σ_w/MPa: 0.12 (*1*), 0.14 (*2*), 0.16 (*3*), 0.18 (*4*), 0.20 (*5*), 0.22 (*6*) and 0.24 (*7*). Experimental data demonstrate an increase in the slopes with increasing shear stresses.

Experimental proof of the ability of DNA solutions to slip along solid walls obtained by fluorescence microscopy is of prime importance.[268, 269] The spatial resolution of the experiment was better than 1 μm.[268] It was found that slip, like in the case of polymer melts, arises at the Weissenberg numbers Wi > 1 and the slip length depends on Wi. Thus slip is indeed determined by the relaxation properties of macromolecules, although no sharp transition to slip does occur in solutions as compared to melts.

4.3. Conformations of macromolecules near solid wall

Understanding physicochemical processes occurring between the fluid and solid wall requires knowledge of the of the slip velocity V_w on stress. There are theoretical grounds[16] to believe that slip under capillary flow of a polymer occurs at any arbitrarily low shear stress. In the framework of the Doi–Edwards model, this can be explained by disentanglement of macromolecules from the entanglement network and subsequent orientation in the flow.[270] A schematic illustration of the phenomenon is presented in Fig. 38.[271]

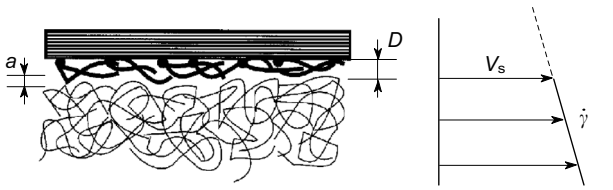


Figure 38. Formation of a near-wall layer of entanglement-free macromolecules of thickness a, which approximately corresponds, in order of magnitude, to the Doi–Edwards 'tube' diameter (D).[271]

This model for slip mechanism represents an alternative to the idea of tightening of knots in the entanglement network, according to which slip is due to the flow–rubbery transition of the polymer. It is believed that this contradiction can be to some extent removed assuming that the 'tube' model is valid for certain chain segments rather than the entire macromolecule, so only particular molecular fragments undergo orientation.

However, central for the present discussion is the so-called strong slip manifesting itself above a certain critical shear stress σ_c, rather than weak slip at low flow velocities. This phenomenon was observed for various polymer melts and has been a subject of several publications (see, *e.g.*, reviews [13, 15–18]).

Numerous measurements showed that the dependence of the slip velocity on the shear stress can be approximated by the following power function:

$$V_w \propto (\sigma_w - \sigma_c)^n \tag{57}$$

with the exponent n lying in the range from 2.5 to 3.3 [*cf.* expression (40)].[251, 264–266] Besides, experiments showed that the slip velocity depends on the molecular characteristics of polymers, *viz.*, the mass-average molecular mass and the width of the MMD.[251, 263, 272, 273] Probably, this is related to flow fractionation of polydisperse polymers.[277]

4.4. Self-oscillations of deformable melts

Slip of a viscoelastic fluid along a solid wall can be followed by the onset of stick–slip self-oscillations. This phenomenon is associated with stress relaxation upon detachment from the surface which causes sticking to the wall and a new stick–slip transition upon accumulation of necessary elastic deformations. Then the process is repeated. Thus, self-oscillations are driven by cyclic flow–slip–flow transitions related to periodic flow–rubbery transitions and *vice versa*. This phenomenon is a specific type of instability under flow of viscoelastic fluids. It was described in numerous studies (see, *e.g.*, Refs 250 and 274–282). For an observer, the stick–slip self-oscillations appear as periodic oscillations of the volumetric flow rate and(or) pressure accompanied by the formation of periodic surface defects. The volumetric flow rate also periodically changes with time while maintaining the specified 'average' flow velocity. The attractor describing the process in question and the schematic diagram of pressure self-oscillations are shown in Fig. 39.

Thus, the slip–stick self-oscillations represent a characteristic bifurcation in the behaviour of the system, originating from coexistence of two (flow and rubbery) relaxation states of the polymer. Visual observation of defects on the surface of the polymer jet precedes the onset of slip. Discontinuities on the surface of polymer jet are due to singularities in the stress field at the channel outlet where the fluid is no longer confined by the solid surface and is transformed to a free jet. The process is accompanied by the development of high normal stresses responsible for the appearance of discontinuities in the polymer jet.[283] This mechanical picture of the primary appearance of defects preceding the slip–stick inside the channel was confirmed by direct measurements of stress distribution along the channel.[284–286] The development of periodicity of defects on the surface of the flowing viscoelastic fluid jet with increasing flow velocity is demonstrated in Fig. 40.[287] One can see that regular defects originating from periodic slip–flow are developed gradually. The amplitude of oscillations is determined by the Weissenberg number as the key characteristic of viscoelastic fluid flow.[282, 288]

An example of periodic slip–stick is shown in Fig. 41 where the surface regions corresponding to different types of motion (flow or slip) are clearly seen.[289]

The concept of periodic slip–flow oscillations is schematically illustrated in Fig. 42. A scraper moving on the viscoelastic surface clings to the material on the surface and drags it, so a crest is formed. As the elastic deformation

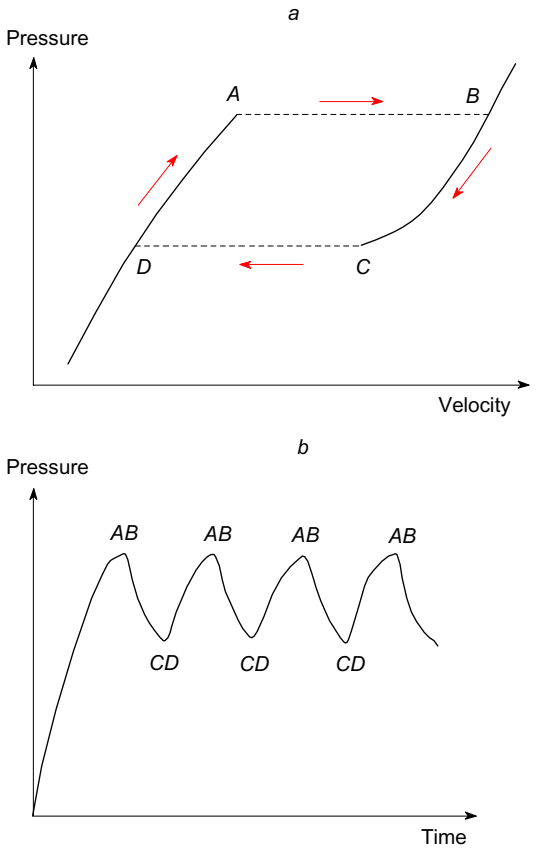


Figure 39. Hysteresis loop observed upon onset of slip–stick effect (*a*) and a pattern of pressure self-oscillations at a specified 'average' volumetric flow rate when a viscoelastic fluid is extruded through a capillary (*b*).

reaches a certain limiting value, the material breaks away, slows down and the scraper slides on the surface for some time. Then the scraper again clings to the viscoelastic fluid and the process is repeated. This type of relative motion of the fluid and the solid surface is realized in capillary channels (the fluid is the moving component while the solid surface is the fixed component).

An increase in the flow velocity is accompanied by the development of instabilities and by the onset of elastic turbulence (combination of wall slip and stochastic motions in the bulk of the fluid resulting in random flow disconti-

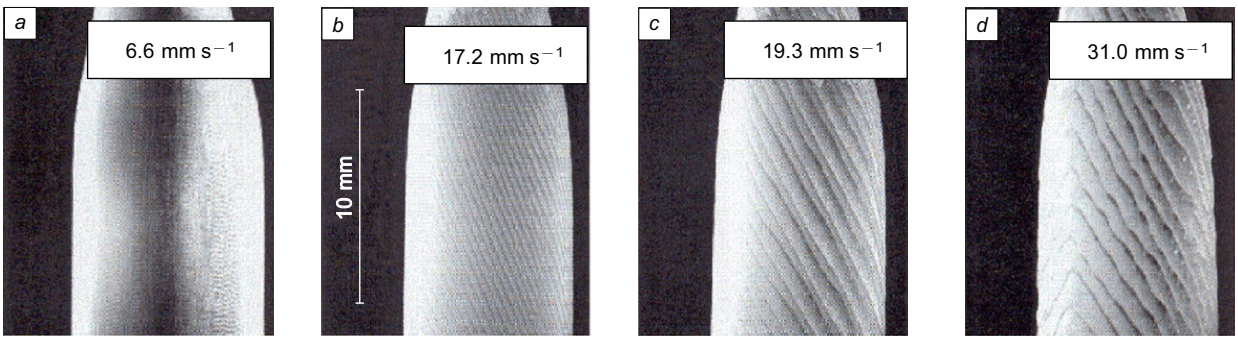


Figure 40. Development of regular defect structure on the surface of viscoelastic fluid jet with increasing the flow velocity of linear polyethylene from 6.6 to 31.0 mm s^{-1} (*a*–*d*) in the slip–stick regime.[287] Capillary dimensions: 6 × 32 mm.

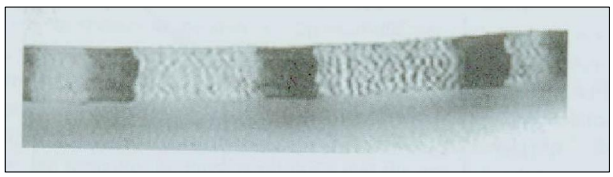


Figure 41. Periodic alternating arrangement of smooth and defect areas of the surface of a polymer jet, corresponding to different types of motion, *viz*., flow (dark smooth areas) and slip in the self-oscillation regime (bright rough areas) when a polymer melt is extruded through a capillary 2 mm in diameter.[289]

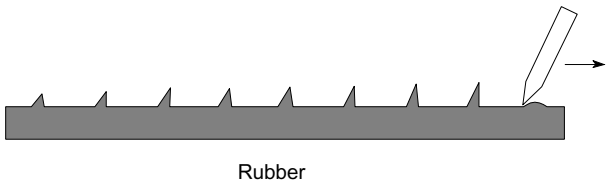


Figure 42. A scheme illustrating the onset of periodic stick–slip oscillations during the motion of viscoelastic fluid.

nuities).[290] This phenomenon has been repeatedly described in original publications.[291–293]

4.5. The role of the surface nature

The main physical mechanism of flow breakdown and periodic slip–stick oscillations is due to the elasticity of the flowing fluid, which leads to relaxation type flow–rubbery transition and back relaxation. However, pushing away from the wall should depend on the interaction at the polymer/wall interaction, so the nature of the wall surface should play a certain role.

High impact of interfacial molecular interactions with emphasis placed on the role of MMD (especially, contributions of high-molecular-mass 'tails', macromolecular architecture, temperature) and surface defects was confirmed in many studies. Since these factors are crucially important to the quality of extrudate, there is huge body of information in this field. Besides, experiments showed that the slip conditions depend on the nature of the solid material contacting the flowing polymer melt. The simplest examples are provided by coating the capillary surface with various adhesives and diffusion of low-molecular-mass (low-viscous) fractions towards the wall.[16, 276, 287]

Even if we ignore the formation of thin low-viscous near-wall layer, it is the nature of the wall material that is of vital importance in the light of the issue discussed. The quality of the surface of the flowing polymer jet depends on the capillary material (see, *e.g*., Ref. 280). Undoubtedly, adhesive interactions between the polymer and the wall should be taken into account when considering the flow–slip transition. For instance, it was assumed[294] that the critical stress corresponding to the onset of slip depends on the work of adhesion. Direct proofs of the role of the nature of the wall are presented in Fig. 43.[295] Clearly, an increase in the work of adhesion surface leads to a marked increase in the critical stress and thus to extension of the no-slip region.

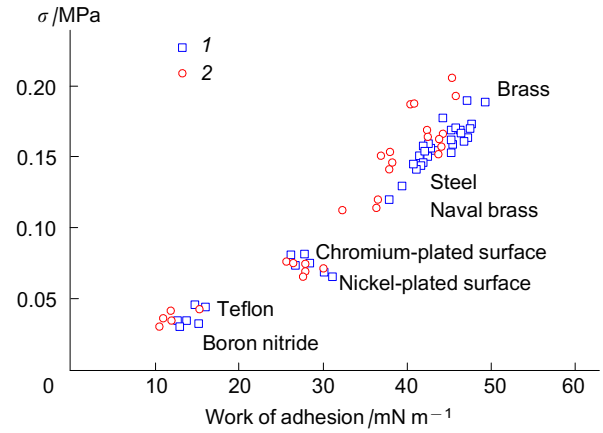


Figure 43. Critical shear stress corresponding to the onset of flow instability for polyethylenes plotted *vs*. work of adhesion of the solid surface.[295]
High-density polyethylene (*1*) and low-density polyethylene (*2*).

The strength of an adhesive contact depends on the pressure produced to create the contact. Therefore, the critical stress at which the fluid breaks away from the wall upon the onset of slip depends on the hydrostatic pressure. The critical stresses under simple shear (without pressure) and under pressure can be compared by analyzing the experimental data presented in Fig. 44 (see Ref. 296) that clearly demonstrates the role of hydrostatic pressure in the onset of slip of the solid surface.

Summing up, shear deformations of polymer melts representing elastic fluids are accompanied by the onset of slip as a result of relaxation-type flow–rubbery transition that is governed by the critical Weissenberg number, *viz*., at higher Weissenberg numbers the melt behaves as a solid. Particular realization of the phenomenon (either continuous slip or slip–stick self-oscillations) is determined by the interfacial interaction between the fluid and the wall.

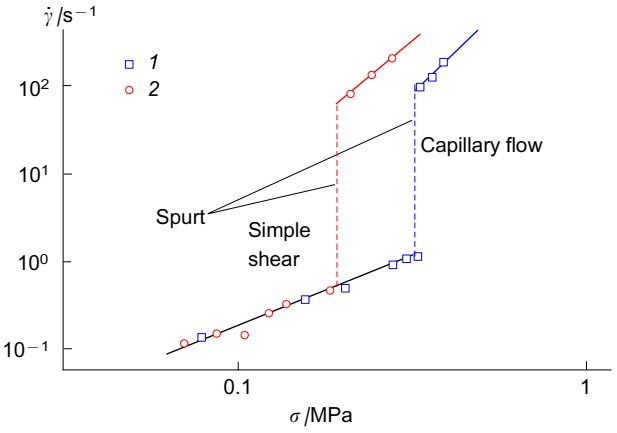


Figure 44. Spurt (onset of slip) under simple shear (no pressure) and capillary flow (under pressure).[296]
High-density polyethylene (*1*) and low-density polyethylene (*2*).

5. Conclusion

Classical textbooks and monographs on the continuum dynamics begin with the balance equations and description of the boundary conditions that are necessary to solve particular problems. When posing and solving dynamic problems, it is hard to find other boundary conditions except the no-slip condition for the fluid near solid interface to be treated as a physical law. However, it was Claude-Louis Navier, the founder of the classical dynamics of viscous fluids, who assumed that, in principle, the possibility for a fluid to slip on the solid boundary (wall) should not be excluded. This phenomenon is characterized by either a certain slip length (it is conditionally determined by extrapolating the actual linear flow velocity profile to a distance corresponding to zero velocity) or by the slip velocity that is determined by the friction coefficient. Indeed, there are physicochemical grounds for the onset of slip of a fluid on the solid surface. In particular, slip can be due to the formation of microcavities on the surface, thus being governed by the energy of the interaction between the fluid and the surface and by the surface roughness. Long-lived gas nanobubbles can exist or be formed in the near-boundary region of the fluid; these bubbles change the physical properties of the near-surface fluid layer. Other slip mechanisms are also possible. Recently, this problem became of particular importance in connection with modern interest in superfluidity and superhydrophobic surfaces. It was found that the slip length can be very large. Taking into account this result, there are various theoretical, experimental and applied aspects related to the physicochemical phenomena at the fluid/solid interface.

Considering flow of multicomponent systems (dispersions of solid particles and colloidal solutions), there are two physical properties of the medium underlying wall slip. The first, most evident property, is the viscoplasticity of a material that can exist in two states and behave like a solid under low shear stress and like a fluid under high stress. Transition from the solid-like to the liquid state occurs at certain critical stress called the yield stress. This transition is not necessary sharp, it can be thixotropic in character and depend on the load (rest) time. Next, a solid-like structure can form at high stresses or deformations of highly concentrated dispersions owing to strain trapping (analogue to vitrification). This makes internal motions of stuctural fragments of the medium impossible and it can move only by the slip mechanism as a solid. In addition, the formation of inhomogeneous structure with a thin low-viscous near-wall fluid layer as particular component is possible. High shear rates in this layer look like as effective slip.

The main mechanism responsible for the possibility of slip of polymer melts is determined by their viscoelastic properties. At sufficiently high deformation rates, a relaxation-type flow – rubbery transition occurs as the critical Weissenberg number is reached. This parameter is responsible for the balance between viscous and elastic deformations of a material. The conditions for the onset and specific features of slip (either continuous or self-oscillating) also depend on the physicochemical features of the interaction between the polymer melt and the wall.

The review has been written with the financial support from the Russian Foundation for Basic Research (Projects No. 18-29-17002 and No. 18-53-15013). It was also supported in part through a grant within the framework of the State Assignment under Contract No. 0082-2014-0013 and the State Program of TIPS RAS.

Figures 1, 7 and 24*a* are courtesy of the American Chemical Society. Figures 2*b*, 3 – 5, 8*d*, 12, 15*b*, 16, 22*b*, 24*b*, 25 and 27 are courtesy of the American Physical Society. Figures 2*a*, 10, 18*b*, 20, 22*a*, 23, 26, 29, 38 and 40 are courtesy of Springer Nature. Figures 6, 28*a*,*b*, 33, 36, 41, 43 and 44 are courtesy of AIP Publishing. Figures 8*a*,*b*,*f*, 21 and 35 are courtesy of Elsevier. Figures 8*e* and 13 are courtesy of the Royal Society of Chemistry (Great Britain). Figure 9*b* is courtesy of Cambridge University Press. Figures 11 and 18*a* are courtesy of IOP Publishing. Figure 14 is courtesy of the National Academy of Sciences of the United States of America. Figure 32 is courtesy of Wiley.

References

1. R.B.Bird, A.E.Stewart. *Transport Phenomena*. (New York: Wiley, 2007)
2. B.R.Munson, A.P.Rothmayer, Th.H.Okiishi, W.W.Huebsch. *Fundamentals of Fluid Mechanics*. (New York: Wiley, 2012)
3. C.L.M.H.Navier. *Mem. Acad. R. Sci. Inst. France*, **1**, 389 (1823)
4. L.Bocquet, J.-L.Barrat. *Soft Matter*, **3**, 685 (2007)
5. A.Karnis, H.L.Goldsmith, S.G.Mason. *Can. J. Chem. Eng.*, **44**, 181 (1966)
6. P.J.A.Hartman Kok, S.G.Kazarian, C.J.Lawrence, B.J.Briskoe. *J. Rheol.*, **46**, 481 (2002)
7. O.I.Vinogradova. *Langmuir*, **11**, 2213 (1995)
8. N.Mooney. *J. Rheol.*, **2**, 210 (1931)
9. D.M.Tolstoi. *Dokl. Akad. Nauk SSSR,* **85**, 1089 (1952)
10. N.V.Churaev, V.D.Sobolev. A N.Somov. *J. Colloid Interface Sci.*, **97**, 574 (1984)
11. T.D.Blake. *Colloids Surf.*, **47**, 135 (1990)
12. *Modern Developments in Fluid Dynamics*. Vol. 2. (Ed. S.Goldstein). (Oxford: Oxford Claredon Press, 1938). P. 676
13. H.A.Barnes. *J. Non-Newton. Fluid Mech.*, **56**, 221 (1995)
14. R.G.Larson. *Rheol. Acta*, **31**, 213 (1992)
15. M.M.Denn. *Annu. Rev. Fluid Mech.*, **33**, 265 (2001)
16. S.G.Hatzikiriakos. *Prog. Polym. Sci.*, **37**, 624 (2001)
17. P.Coussot. *J. Non-Newton. Fluid Mech.*, **211**, 31 (2014)
18. M.Cloitre, R.T.Bonnecaze. *Rheol. Acta*, **56**, 283 (2017)
19. J.-L.Barrat, L.Bocquet. *Phys. Rev. Lett.*, **82**, 4671 (1999)
20. J.S.Rowlinson. B.Widom. *Molecular Theory of Capillarity*. (Oxford: Oxford University Press, 1989)
21. Ch.Sendner, D.Horinek, L.Bocquet, R.R.Netz. *Langmuir*, **25**, 10768 (2009)
22. N.V.Priezjev, S.M.Troian. *Phys. Rev. Lett.*, **92,** 018302 (2004)
23. P.A.Thompson, S.M.Troian. *Nature (London)*, **389**, 360 (1997)
24. Y.Zhu, S.Granick. *Phys. Rev. Lett.*, **87,** 096105 (2001)
25. V.S.J.Craig, C.Neto, D.R.M.Williams. *Phys. Rev. Lett.*, **87** 054504 (2001)
26. C.Neto, V.S.J.Craig, D.R.M.Williams. *Eur. Phys. J., E*, **12,** 71 (2003)
27. S.Guriyanova, B.Semin, T.S.Rodrigues, H.-J.Butt, E.Bonaccurso. *Microfluid. Nanofluid.*, **8**, 653 (2010)
28. Y.Zhu, S.Granick. *Macromolecules*, **35**, 4658 (2002)
29. Y.Zhu, S.Granick. *Phys. Rev. Lett.*, **88,** 106102 (2002)
30. S.Granick, Y.Zhu, H.Lee. *Nat. Mater.*, **2**, 221 (2003)

31. C.Cottin-Bizonne, B.Cross, A.Steinberger, E.Charlaix. *Phys. Rev. Lett.*, **94**, 056102 (2005)
32. L.Joly, C.Ybert, L.Bocquet. *Phys. Rev. Lett.*, **96**, 046101 (2006)
33. P.de Gennes. *Langmuir*, **18**, 3413 (2002)
34. C.-H.Choi, K.J.A.Westin, K.S.Breuer. *Phys. Fluids*, **15**, 2897 (2003)
35. O.I.Vinogradova, K.Koynov, A.Best, F.Feuillebois. *Phys. Rev. Lett.*, **102**, 118302 (2009)
36. D.C.Tretheway, C.D.Meinhart. *Phys. Fluids*, **14**, L9 (2002)
37. S.B.Ramisetti, M.K.Borg, D.A.Lockerby, J.M.Reese. *Phys. Rev. Fluids*, **2**, 084003 (2017)
38. T.V.Nizkaya, E.S.Asmolov, O.I.Vinogradova. *Soft Matter*, **9**, 11671 (2013)
39. T.V.Nizkaya, E.S. Asmolov, O.I.Vinogradova. *Phys. Rev. E*, **90**, 043017 (2014)
40. E.Lauga, M.P.Brenner. *Phys. Rev. E*, **70**, 026311 (2004)
41. S.Lou, Z.Ouyang, Y.Zhang, X.Li, J.Hu, M.Li, F.Yang. *J. Vac. Sci. Technol., B*, **18**, 2573 (2000)
42. N.Ishida, T.Inoue, M.Miyahara, K.Higashitani. *Langmuir*, **16**, 6377 (2000)
43. J.W.G.Tyrrell, P.Attard. *Phys. Rev. Lett.*, **87**, 176104 (2001)
44. J.W.G.Tyrrell, P.Attard. *Langmuir*, **18**, 160 (2002)
45. J.Yang, J.Duan, D.Fornasiero, J.Ralston. *J. Phys. Chem. B*, **107**, 6139 (2003)
46. X.H.Zhang, A.Quinn, W.A.Ducker. *Langmuir*, **24**, 4756 (2008)
47. V.Stuart, J.Craig. *Soft Matter*, **7**, 40 (2011)
48. J.R.T.Seddon, D.Lohse. *J. Phys.: Condens. Matter*, **23**, 133001 (2011)
49. Y.Wang, H.Wang, S.Bi, B.Guo. *J. Nanotechnol.*, **56**, 952 (2015)
50. C.-K.Fang, H.-C.Ko, C.-W.Yang, Y.-H.Lu, I.-S.Hwang. *Sci. Rep.*, **6**, 24651 (2016)
51. D.Li, D.Jing, Y.Pan, B.Bhushan, X.Zhao. *Langmuir*, **32**, 11287 (2016)
52. A.C.Simonsen, P.L.Hansen, B.Klösgen. *J. Colloid Interface Sci.,* **273,** 291 (2004)
53. M.Switkes, J.W.Ruberti. *Appl. Phys. Lett.*, **84**, 4759 (2004)
54. Z.P.Du, M.P.Bilbao-Montoya, B.P.Binks, E.Dickinson, R.Ettelaie, B.S.Murray. *Langmuir*, **19.** 3106 (2003)
55. V.Mhetar, L.A.Archer. *Macromolecules*, **31**, 8617 (1998)
56. P.Attard. *Adv. Colloid Interface Sci.*, **104**, 75 (2003)
57. H.-J.Butt, B.Cappella. M.Kappl. *Surf. Sci. Rep.*, **59**, 1 (2005)
58. X.H.Zhang, X.D.Zhang, S.T.Lou, Z.X.Zhang, J.L.Sun, J.Hu. *Langmuir*, **20**, 3813 (2004)
59. X.H.Zhang, N.Maeda, V.S.J.Craig. *Langmuir*, **22**, 5025 (2006)
60. S.Ljunggren, J.C.Eriksson. *Colloids Surf., A*, **129** – **130**, 151 (1997)
61. M.P.Brenner, D.Lohse. *Phys. Rev. Lett.*, **101**, 214505 (2008)
62. X.Zhang, M.H.Uddin, H.Yang, G.Toikka, W.Ducker, N.Maeda. *Langmuir*, **28**, 10471 (2012)
63. H.A.Pacheco-Martinez, L.Liao, R.J.A.Hill, M.R.Swift, R.M.Bowley. *Phys. Rev. Lett.*, **110** 154501 (2013)
64. H.P.Fang, J.Hu. *Nucl. Sci. Tech.*, **17**, 71 (2006)
65. L.J.Zhang, H.Chen, Z.X.Li, H.P.Fang, L.Hu. *Sci. China, G: Phys., Mechan., Astron.*, **51**, 219 (2008)
66. E.Bonaccurso, H.-J.Butt,V.S.J.Craig. *Phys. Rev. Lett.*, **90**, 144501 (2003)
67. S.C.Yang, L.B.Fang. *Mol. Simulat.*, **31**, 971 (2005)
68. O.A.Kozaderov. *Kondens. Sredy Mezhfaz. Granitsy*, **19**, 6 (2017)
69. A.Niavarani, N.V.Priezjev. *Phys. Rev. E*, **81**, 011606 (2010)
70. N.V.Priezjev, S.Troian. *J. Fluid Mech.*, **554**, 25 (2006)
71. A.Niavarani, N.V.Priezjev. *J. Chem. Phys.*, **129**, 144902 (2008)
72. C.Zhang, Y.Chen. *Chem. Eng. Proc.*, **85**, 203 (2014)
73. S.Richardson. *J. Fluid Mech.*, **59**, 707 (1973)
74. M.Papanikolaou, M.Frank, D.Drikakis. *Phys. Fluids*, **28**, 082001 (2016)
75. S.Richardson. *J. Fluid Mech.*, **49**, 327 (1971)
76. C.Y.Wang. *Phys. Fluids*, **15**, 1114 (2003)
77. A.D.Stroock, S.K.Dertinger, G.M.Whitesides, A.Adjari. *Anal. Chem.*, **74**, 5306 (2002)
78. O.I.Vinogradova, G.E.Yakubov. *Phys. Rev. E*, **73**, 045302 (R) (2006)
79. C.Kunert, J.Harting, O.I.Vinogradova. *Phys. Rev. Lett.*, **105**, 016001 (2010)
80. C.Kunert, J.Harting. *Phys. Rev. Lett.*, **99**, 176001 (2007)
81. C.Kunert, J.Harting. *Int. J. Comput. Fluid Dynam.*, **22**, 475 (2008)
82. J.Sanchez-Reyes, L.A.Archer. *J. Rheol.*, **46**, 1239 (2002)
83. J. Sanchez-Reyes, L.A.Archer. *Langmuir*, **19**, 3304 (2003)
84. R.N.Wenzel. *Ind. Eng. Chem.*, **28**, 988 (1936)
85. I.V.Kravchenko, S.A.Patlazhan. *Polym. Sci., Ser. A*, **51,** 923 (2009)
86. A.B.D. Cassie, S.Baxter. *Trans. Faraday Soc.*, **40**, 546 (1944)
87. T.Onda, S.Shibuichi, N.Satoh, K.Tsujii. *Langmuir*, **12,** 2125 (1996)
88. https://www.suckerpunchdaily.com/2010/04/05/sleeping-insects-covered-in-dew/ (5.09.2018)
89. S.S.Latthe, C.Terashima, K.Nakata, A.Fujishima. *Molecules*, **19**, 4256 (2014)
90. Y.Zheng. *Bio-Inspired Wettability Surfaces: Developments in Micro- and Nanostructures*. (Singapore: Pan Stanford Publishing, 2015)
91. A.Tripathy, P.Sen, B.Su, W.H.Briscoe. *Adv. Colloid Interface Sci.*, **248**, 85 (2017)
92. S.S.Latthe, A.B.Gurav, C.S.Maruti, R.S.Vhatkar. *J. Surf. Eng. Mater. Adv. Technol.*, **2**, 76 (2012)
93. J.T.Simpson, S.R.Hunter, T.Aytug. *Rep. Prog. Phys.*, **78**, 086501 (2015)
94. L.R.J.Scarratt, U.Steiner, C.Neto. *Adv. Colloid Interface Sci.*, **246**, 133 (2017)
95. K.Koch, B.Bhushan, W.Barthlott. *Prog. Mater. Sci.*, **54**, 137 (2009)
96. C.Lee, C.Choi, C.Kim. *Phys. Rev. Lett.*, **101**, 064501 (2008)
97. T.V.Nizkaya, A.L.Dubov, A.Mourran, O.I.Vinogradova. *Soft Matter*, **12**, 6910 (2016)
98. A.Marmur. *Langmuir*, **19**, 834 (2003)
99. E.Bormashenko. *Wetting of Real Surfaces. Series: De Gruyter Studies in Mathematical Physics*. Vol. 19. (Berlin, Boston: Walter de Gruyter, 2013)
100. W.Choi, A.Tuteja, J.M.Mabry, R.E.Cohen, G.H.McKinle. *J. Colloid Interface Sci.*, **339**, 208 (2009)
101. E.Jenner, B.D'Urso. *Appl. Phys. Lett.*, **103**, 251606 (2013)
102. E.Jenner, C.Barbier, B.D'Urso. *Appl. Surf. Sci.*, **282**, 73 (2013)
103. R.Jain, R.Pitchumani. *Langmuir*, **33**, 7181 (2017)
104. G.McHale. *Langmuir*, **23**, 8200 (2007)
105. H.A.Stone, A.D.Stroock, A.Ajdari. *Ann. Rev. Fluid Mech.*, **36**, 381 (2004)
106. M.Z.Bazant, O.I.Vinogradova. *J. Fluid Mech.*, **613**, 125 (2008)
107. F.Feuillebois, M.Z.Bazant, O.I.Vinogradova. *Phys. Rev. Lett.*, **102**, 026001 (2009)
108. K.Kamrin, M.Z.Bazant, H.A.Stone. *J. Fluid Mech.*, **658**, 409 (2010)
109. J.R.Philip. *Z. Angew. Math. Phys.*, **23**, 353 (1972)
110. E.Lauga, H.A.Stone. *J. Fluid Mech.*, **489**, 55 (2003)

111. E.S.Asmolov, O.I.Vinogradova. *J. Fluid Mech.*, **706**, 108 (2012)
112. C.Cottin-Bizonne, C.Barentin, L.Bocquet. *Phys. Fluids*, **24**, 012001 (2012)
113. A.V.Belyaev, O.I.Vinogradova. *Soft Matter*, **6**, 4563 (2010)
114. A.V.Belyaev, O.I.Vinogradova. *J. Fluid Mech.*, **652**, 489 (2010)
115. O.I.Vinogradova, A.V.Belyaev. *J. Phys.: Condens. Matter*, **23** 184104 (2011)
116. S.A.Vagner. S.A.Patlazhan. *Dokl. Phys. Chem.*, **459**, 203 (2014)
117. J.Ou, G.R.Moss, J.P.Rothstein. *Phys. Rev. E*, **76**, 016304 (2007)
118. S.A.Vagner, S.A.Patlazhan. *J. Phys.: Conf. Ser.*, **774**, 012027 (2016)
119. M.Sbragaglia, A.Prosperetti. *Phys. Fluids*, **19**, 043603 (2007)
120. J.Ou, B.Perot, J.P.Rothstein. *Phys. Fluids*, **16**, 4635 (2004)
121. P.Lv, Y.Xue, Y.Shi, Y.H.Lin, H.Duan. *Phys. Rev. Lett.*, **112**, 196101 (2014)
122. Y.Xiang, Y.Xue, P.Lv, D.Li, H.Duan. *Soft Matter*, **12**, 4241 (2016)
123. A.S.Haase, E.Karatay, P.A.Tsai, R.G.H.Lammertink. *Soft Matter*, **9**, 8949 (2013)
124. B.H.Kwon, H.H.Kim, H.J.Jeon, M.C.Kim, I.Lee, S.Chun, J.S.Go. *Exp. Fluids*, **55**, 1 (2014)
125. B.N.Jagdish, T.Z.X.Brandon, T.J.Kwee, A.K.Dev. *J. Ship Res.*, **58**, 30 (2014)
126. B.Wang, J.Wang, Z.Dou, D.Chen. *Ocean Eng.*, **79**, 58 (2014)
127. P.Du, J.Wen, Z.Zhang, D.Song, A.Ouahsine, H.Hu. *Ocean Eng.*, **130**, 328 (2017)
128. J.Bico, U.Thiele, D.Quéré. *Colloids Surf., A*, **206**, 41 (2002)
129. G.Whyman, E.Bormashenko. *Langmuir*, **27**, 8171 (2011)
130. E.Bormashenko. *Adv. Colloid Interface Sci.*, **222**, 92 (2015)
131. E.Bormashenko. *Low Temp. Phys.*, **42**, 622 (2016)
132. Q.-S.Zheng, Y.Yu, Z.-H.Zhao. *Langmuir*, **21**, 12207 (2005)
133. D.Bartolo, F.Bouamrirene, E.Verneuil, A.Buguin, B.Silberzan, S.Moulinet. *Europhys. Lett.*, **74**, 299 (2006)
134. Z.Yoshimitsu, A.Nakajima, T.Watanabe, K.Hashimoto. *Langmuir*, **18**, 5818 (2002)
135. B.Emami, A.A.Hemeda, M.M.Amrei, A.Luzar, M.Gad-el-Hak, H.V.Tafreshi. *Phys. Fluids*, **25**, 062108 (2013)
136. R.Poetes, K.Holtzmann, K.Franze, U.Steiner. *Phys. Rev. Lett.*, **105**, 166104 (2010)
137. E.Bormashenko, A.Musin, G.Whyman, M.Zinigrad. *Langmuir*, **28**, 3460 (2012)
138. A.Steinberger, C.Cottin-Bizonne, P.Kleimann, E.Charlaix. *Nat. Mater.*, **6**, 665 (2007)
139. J.Hyväluoma, J.Harting. *Phys. Rev. Lett.*, **100**, 246001 (2008)
140. A.M.J.Davis, E.Lauga. *Phys. Fluids*, **21**, 011701 (2009)
141. E.Karatay, A.S.Haase, C.W.Visser, C.Sun, D.Lohse, P.A.Tsai, R.G.H.Lammertink. *Proc. Natl. Ac. Sci.*, **110**, 8422 (2013)
142. Y.Li, K.Alame, K.Mahesh. *Phys. Rev. Fluids*, **2**, 054002 (2007)
143. D.Crowdy. *Phys. Fluids*, **29**, 091702 (2017)
144. A.S.Haase, J.A.Wood, L.M.J.Sprakel,, R.G.H.Lammertink. *Phys. Rev. E*, **95**, 023105 (2017)
145. C.-O.Ng, C.Y.Wang. *Phys. Fluids*, **21**, 013602 (2009)
146. C.J.Teo, B.C.Khoo. *Microfluid. Nanofluid.*, **9**, 499 (2010)
147. S.Patlazhan, S.Vagner. *Phys. Rev. E*, **96**, 013104 (2017)
148. D.Crowdy. *Phys. Rev. Fluids*, **2**, 124201 (2017)
149. K.Yasuda, R.C.Armstrong, R.E.Cohen. *Rheol. Acta*, **20**, 163 (1981)
150. A.Ya.Malkin, V.G.Kulichikhin, S.O.Ilyin. *Rheol. Acta*, **56**, 177 (2017)
151. D.Vlassopoulos, M.Cloitre. *Curr. Opin. Colloid Interface Sci.*, **19**, 561 (2014)
152. AYa.Malkin, V.G.Kulichikhin. *Russ. Chem. Rev.*, **84**, 803 (2015)
153. R.Foudazi, S.Qavi, I.Masalova, A.Ya.Malkin. *Adv. Colloid Interface Sci.*, **220**, 78 (2015)
154. R.Buscall, J.I.McGowan, A.J.Morton-Jones. *J. Rheol.*, **37**, 621 (1993)
155. W.B.Russel, M.C.Grant. *Colloids Surf., A*, **161**, 271 (2000)
156. H.J.Walls, S.B.Caines, A.M.Sanchez, S.A.Khan. *J. Rheol.*, **47**, 847 (2003)
157. T.Gibaud, D.Frelat, S.Manneville. *Soft Matter*, **6**, 3482 (2010)
158. M.Laurati, S.U.Egelhaaf, G.Petekidis. *J. Rheol.*, **55**, 673 (2011)
159. P.Ballesta, N.Koumakis, R.Besseling, W.C.K.Poon, G.Petekidis. *Soft Matter*, **9**, 3237 (2013)
160. H.M.Princen, A.D.Kiss. *J. Colloid Interface Sci.*, **112**, 427 (1986)
161. T.G.Mason, J.Bibette, D.A.Weitz. *J. Colloid Interface Sci.*, **179**, 439 (1996)
162. T.G.Mason, M.-D.Lacasse, G.S.Grest, D.Levine, J.Bibette, D.A.Weitz. *Phys. Rev. E*, **56**, 3150 (1997)
163. J.R.Seth, L.Mohan, C.Locatelli-Champagne, M.Cloitre, R.T.Bonnecaze. *Nat. Mater.*, **10**, 838 (2011)
164. I.Masalova, R.Foudazi, A.Ya.Malkin. *Colloids Surf., A*, **375**, 76 (2011)
165. P.Menut, S.Seiffert, J.Sprakelae, D.A.Weitz. *Soft Matter*, **8**, 156 (2012)
166. *Microgel Suspensions: Fundamentals and Applications*. (Eds A.Fernandez-Nieves, H.Wyss, J.Mattsson, D.A.Weitz). (Weinheim: Wiley, 2011)
167. D.Vlassopoulos, G.Fytas, T.Pakula, J.Roovers. *J. Phys.: Condens. Matter*, **13**, R855 (2001)
168. R.Foudazi, I.Masalova, A.Ya.Malkin. *Colloid J.*, **72**, 74 (2010)
169. J.B.Sokoloff. *J. Chem. Phys.*, **142**, 234903 (2015)
170. D.Abreu, M.Levant, V.Steinberg, U.Seifert. *Adv. Colloid Interface Sci.*, **208**, 129 (2014)
171. B.P.Binks, R.Murakami. *Nat. Mater.*, **5**, 865 (2006)
172. E.Bormashenko. *Curr. Opin. Colloid Interface Sci.*, **16**, 266 (2011)
173. E.Bormashenko, G.Whyman, O.Gendelman. *Adv. Cond. Matter Phys.*, **2015**, 206578 (2015)
174. E.Bormashenko, Y.Bormashenko, R.Grynyov, H.Aharoni, G.Whyman, B.P.Binks. *J. Phys. Chem. C*, **119**, 9910 (2015)
175. C.H.Ooi, C.Plackowski, A.V.Nguyen, R.K.Vadivelu, J.A.St.John, D.V.Dao. N.-T.Nguyen. *Sci. Rep.*, **6**, 21777 (2016)
176. W.B.Russel, D.A.Saville, W.R.Schowalter. *Colloidal Dispersions*. Cambridge University Press, New York, 1989
177. J.Mewis, N.J.Wagner. *Colloidal Suspension Rheology*. (New York: Cambridge University Press, 2012)
178. P.G.De Gennes, J.Prost. *Physics of Liquid Crystals*. (Oxford: Oxford University Press, 1994)
179. R.T.Bonnecaze, M.Cloitre. *Adv. Polym. Sci.*, **236**, 117 (2010)
180. S.G.Hatzikiriakos. *Soft Matter*, **11**, 7851 (2015)
181. D.Bonn, M.M.Denn, L.Berthier, T.Divoux, S.Manneville. *Rev. Mod. Phys.*, **89**, 035005 (2017)
182. R.Pal, S.N.Bhattacharya, E.Rhodes. *Can. J. Chem. Eng.*, **64**, 3 (1986)
183. R.Pal. *Colloids Surf., A*, **162**, 55 (2000)
184. I.Masalova, A.Ya.Malkin. *Chem. Eng. Res. Des.*, **91,** 204 (2013)

185. M.Habibi, M.Dinkgreve, J.Paredes, M.M.Denn, D.Bonn. *J. Non-Newton. Fluid Mech.*, **238**, 33 (2016)
186. G.V.Vinogradov, G.B Froishteter, K.K.Trilisky, E.L.Smorodinsky. *Rheol. Acta*, **14**, 765 (1975)
187. P.Ballesta, G.Petekidis, L.Isa, W.C.K.Poon, R.Besseling. *J. Rheol.*, **56**, 1005 (2012)
188. D.M.Kalyon. *J. Rheol.*, **49**, 621 (2005)
189. P.Ballesta, R.Besseling, L.Isa, G.Petekidis, W.C.K.Poon. *Phys. Rev. Lett.*, **101**, 258301 (2008)
190. L.Isa, R.Besseling, A.B.Schofield, W.C.K.Poon. *Adv. Polym. Sci.*, **236**, 163 (2010)
191. S.P.Meeker, R.T.Bonnecaze, M.Cloitre. *Phys. Rev. Lett.*, **92**, 198302 (2004)
192. S.P.Meeker, R.T.Bonnecaze, M.Cloitre. *J. Rheol.*, **48**, 1295 (2004)
193. J.R.Seth, M.Cloitre, R.T.Bonnecaze. *J. Rheol.*, **52**, 1241 (2008)
194. H.M.Shewan, J.R.Stokes, M.Cloitre. *Soft Matter*, **13**, 2099 (2017)
195. J.-M.Piau. *J. Non-Newton Fluid Mech.*, **144**, 1 (2007)
196. A.Poumaere, M.Moyers-González, C.Castelain, T.Burghelea. *J. Non-Newton. Fluid Mech.*, **205**, 284 (2012)
197. J.F.Ortega-Avila, J.Pérez-González, B.M.Marín-Santibáñez, F.Rodríguez-González, S.Aktas, M.Malik, D.M.Kalyon. *J. Rheol.*, **60**, 503 (2016)
198. B.M.Erwin, M.Cloitre, M.Gauthierd, D.Vlassopoulos. *Soft Matter*, **6** 2825 (2010)
199. W.H.Herschel, R.Bulkley. *Kolloid Z.*, **39**, 291 (1926)
200. J.Goyon, A.Colin, G.Ovarlez, A.Ajdari, L.Bocquet. *Nature (London)*, **454**, 84 (2008)
201. P.Schall, D.A.Weitz, F.Spaepen. *Science*, **318**, 1895 (2007)
202. A.Magnin, J.-M. Piau. *J. Non-Newton. Fluid Mech.*, **36**, 85 (1990)
203. A.Ya.Malkin, I.Masalova. *J. Non-Newton. Fluid Mech.*, **147,** 65 (2007)
204. J.R.Seth, C.Locatelli-Champagne, F.Monti, R.T.Bonnecaze, M.Cloitre. *Soft Matter*, **8**, 140 (2012)
205. P.Schall. M.van Hecke. *Annu. Rev. Fluid Mech.*, **42**, 67 (2010)
206. A.Ya.Malkin, A.V.Semakov, V.G.Kulichikhin. *Adv. Colloid Interface Sci.*, **157**, 75 (2010)
207. T.Divoux, M.A.Fardin, S.Manneville, S.Lerouge. *Annu. Rev. Fluid Mech.*, **48**, 81 (2016)
208. L.B.Chen, C.F.Zukoski, B.J.Ackerson, H.J.M.Hanley, G.C.Straty, J.Barker, C.J.Glinka. *Phys. Rev. Lett.*, **69**, 688 (1992)
209. M.E.Helgeson, M.D.Reichert, Y.T.Hu, N.J.Wagner. *Soft Matter*, **5**, 3858 (2009)
210. H.Kawabata, D.Nishiura, H.Sakaguchi, Y.Tatsumi. *Rheol. Acta*, **52**, 1 (2013)
211. G.Ovarlez, S.Rodts, X.Chateau, P.Coussot. *Rheol. Acta*, **48**, 831 (2009)
212. S.Jarny, N.Roussel, S.Rodts, F.Bertrand, R.Le Roy, P.Coussot. *Cement Concr. Res.*, **35**, 1873 (2005)
213. K.Kang, M.P.Lettinga, J.K.G.Dhont. *Rheol. Acta*, **47**, 499 (2008)
214. A.Fall, J.Paredes, D.Bonn. *Phys. Rev. Lett.*, **105**, 225502 (2010)
215. S.A.Rogers, D.Vlassopoulos, P.T.Callaghan. *Phys. Rev. Lett.*, **100**, 128304 (2008)
216. M.A.Fardin, T.Divoux, M.A.Guedeau-Boudeville, I.Buchet-Maulien, J.Browaeys, G.H.McKinley, S.Manneville, S.Lerouge. *Soft Matter*, **8**, 2535 (2012)
217. F.Bautista, J.H.Pérez-López, J.P.García, J.E.Puig, O.Manero. *J. Non-Newton. Fluid Mech.*, **144**, 160 (2007)
218. Y.T.Hu, C.Palla, A.Lips. *J. Rheol.*, **52**, 379 (2008)
219. P.E.Boukany, S.-Q.Wang. *Soft Matter*, **5**, 780 (2009)
220. M.Cromer, G.H.Fredrickson, L.G.Leal. *Phys. Fluids*, **26**, 063101 (2014)
221. S.Cheng, S.-Q.Wang. *J. Rheol.*, **56**, 1413 (2012)
222. S.Jaradat, M.Harvey, T.A.Waigh. *Soft Matter*, **8**, 11677 (2012)
223. P.Tapadia, S.-Q.Wang. *Phys. Rev. Lett.*, **96**, 016001 (2006)
224. S.-Q.Wang, S.Ravindranath, P.E.Boukany. *Macromolecules*, **44**, 183 (2011)
225. M.A.Fardin, T.J.Ober, C.Gay, G.Grégoire, G.H.McKinley, S.Lerouge. *Soft Matter*, **8**, 910 (2012)
226. A.-L.Vayssade, C.Lee, E.Terriac, F.Monti, M.Cloitre, P.Tabeling. *Phys. Rev. E*, **89**, 052309 (2014)
227. S.-Q.Wang. *Nonlinear Polymer Rheology: Macroscopic Phenomenology and Molecular Foundation*. (New York: Wiley, 2017)
228. A.Z.Szeri. *Fluid Film Lubrication*. (Cambridge: Cambridge University Press, 2010)
229. K.L.Johnson. *Contact Mechanics*. (Cambridge: Cambridge University Press, 1985)
230. U.Yilmazer, D.M.Kalyon. *J. Rheol.*, **33**, 1197 (1989)
231. S.C.Jana, B.Kapoor, A.Acrivos. *J. Rheol.*, **39**, 1123 (1995)
232. F.Soltani, U.Yilmazer. *J. Appl. Polym. Sci.*, **70**, 515 (1998)
233. B.K.Aral, D.M.Kalyon. *J. Rheol.*, **38**, 957 (1994)
234. T.Gregory, S.Mayers. *Surf. Coat. Int.*, **76**, 82 (1993)
235. J.M.Franco, C.Gallegos, H.A.Barnes. *J. Food Eng.*, **36**, 89 (1998)
236. S.O.Ilyin, A.Ya.Malkin, V.G.Kulichikhin, A.Yu.Shaulov, E.V.Stegno, A.A.Berlin, S.A.Patlazhan. *Rheol. Acta*, **53**, 467 (2014)
237. G.V.Vinogradov, A.Ya.Malkin, Yu.G.Yanovskii, E.K.Borisenkova, B.V.Yarlykov, G.V.Berezhnaya. *J. Polym. Sci., Part A2*, **10**, 1061 (1972)
238. G.V.Vinogradov. *Pure Appl. Chem.*, **39**, 115 (1974)
239. G.V.Vinogradov. *Polymer*, **18**, 1275 (1977)
240. G.V.Vinogradov, A.Ya.Malkin, V.V.Volosevich. *Appl. Polym. Symp.*, **27**, 47 (1975)
241. A.Ya.Malkin. *Polym. Sci.*, **61**, 80 (2009)
242. A.Ya.Malkin, A.V.Semakov, V.G.Kulichihkin. *Rheol. Acta*, **50**, 485 (2011)
243. A.Ya.Malkin, A.V.Semakov, V.G.Kulichikhin. *Appl. Rheol.*, **22**, 32575 (2012)
244. L.Pérez-Trejo, J.Pérez-González, L.de Vargas, E.Moreno. *Wear*, **259**, 329 (1994)
245. J.Pérez-González. *J. Rheol.*, **45**, 845 (2001)
246. J.Pérez-González. *J. Rheol.*, **49**, 571 (2005)
247. H.E.Park, S.T.Lim, F.Smillo, J.M.Dealy, Ch.G.Robertson. *J. Rheol.*, **53**, 1201 (2008)
248. D.M.Kalyon, H.Gevgilli. *J. Rheol.*, **47**, 683 (2003)
249. S.G.Hatzikiriakos, J.M.Dealy. *J. Rheol.*, **35**, 497 (1991)
250. D.S.Kalika, M.M.Denn. *J. Rheol.*, **31**, 815 (1987)
251. E.Chatzigiannakis, M.Ebrahimi, M.H.Wagner, S.G.Hatzikiriakos. *Rheol Acta*, **56**, 85 (2017)
252. E.K.Borisenkova, G.B.Vasil'ev, V.G.Kulichilhin, D.R.Tur. *Polym. Sci., Sect. A*, **40**, 1112 (1998)
253. H.Münstedt, M.Schmidt, E.Wassner. *J. Rheol.*, **44**, 413 (2000)
254. F.Rodríguez-González, J.Pérez-González, L.de Vargas, B.M.Marín-Santibáñez. *Rheol. Acta*, **49**, 145 (2010)
255. J.Pérez-González, J.J.López-Durán, B.M.Marín-Santibáñez, F.Rodríguez-González. *Rheol. Acta*, **51**, 937 (2012)

256. A.Ya.Malkin, N.K.Blinova, G.V.Vinogradov, M.P.Zabugina, O.Yu.Sabsai, V.C.Shalganova, I.Yu.Kirchevskaya, V.P.Shatalov. *Eur. Polym. J.*, **10**, 445 (1974)
257. A.Ya.Malkin, A.V.Semakov, V.G.Kulichikhin. *Polym. Sci., Sect. A*, **54**, 752 (2012)
258. A.Ya.Malkin. *J. Non-Newton. Fluid Mech.*, **192**, 48 (2013)
259. S.G.Hatzikiriakos, J.M.Dealy. *J. Rheol.*, **36**, 703 (1992)
260. M.Ansari, Y.W.Inn, A.M.Sukhadia, P.J.Des Lauriers, S.G.Hatzikiriakos. *J. Rheol.*, **57**, 927 (2013)
261. M.Ebrahimi, M.Ansari, S.G.Hatzikiriakos. *J. Rheol.*, **59**, 885 (2015)
262. R.Zhao, Ch.W.Macosko. *J. Rheol.*, **46**, 145 (2002)
263. P.Lee, H.E.Park, D.C.Morse, Ch.W.Macosko. *J. Rheol.*, **53**, 893 (2009)
264. G.V.Vinogradov, L.I.Ivanova. *Rheol. Acta*, **7**, 243 (1968)
265. A.V.Ramamurthy. *J. Rheol.*, **30**, 337 (1986)
266. A.Ya.Malkin, A.V.Baranov, N.E.Vikulenkova. *Rheol. Acta*, **32**, 150 (1993)
267. A.Yoshimura, R.K.Prud'homme. *J. Rheol.*, **32**, 53 (1968)
268. P.E.Boukany, O.Hemminger, S.-Q.Wang, L.J.Lee. *Phys. Rev. Lett.*, **105**, 027802 (2010)
269. E.S.G.Shaqfeh. *J. Non-Newton. Fluid Mech.*, **130**, 1 (2006)
270. M.Doi, S.F.Edwards. *The Theory of Polymer Dynamics*. (Oxford; Oxford Science Publication, 1999)
271. S.-Q.Wang. *Adv. Polym. Sci.*, **138**, 227 (1999)
272. N.Othman, B.Jazrawi, S.G.Mehrkhodavandi, S.G.Hatzikiruakos. *Rheol. Acta*, **51**, 357 (2012)
273. M.Ebrahini, M.Ansan, W.Y.Inn, S.G.Hatzikiruakos. *Phys. Fluids*, **28**, 093202 (2016)
274. F.Koran, J.M.Dealy. *J. Rheol.*, **43**, 1291 (1999)
275. T.de Jesús Guadarrama-Medina, J.Pérez-González, L.de Varges. *Rheol. Acta*, **44**, 278 (2005)
276. J.F.Vega, M.T.Expósito, J.Otegui, J.Martínez-Salazar. *J. Rheol.*, **55**, 855 (2011)
277. N.El Kissi, L.Leger, J.-M.Piau, A.Mezghani. *J. Non-Newton. Fluid Mech.*, **52**, 249 (1994)
278. S.-Q.Wang, P.Drda. *Macromolecules*, **29**, 4115 (1996)
279. S.-Q.Wang, P.Drda. *Macromol. Chem. Phys.*, **198,** 673 (1997)
280. V.G.Ghanta, B.L.Riise, M.M.Denn. *J. Rheol.*, **43**, 435 (1999)
281. L.Robert, Y.Demay, B.Vergnes. *Rheol. Acta*, **43**, 89 (2004)
282. E.Miller, J.P.Rothstein. *Rheol. Acta*, **44**, 160 (2004)
283. F.N.Cogswell. *J. Non-Newton. Fluid Mech.*, **2**, 37 (1997)
284. V.I.Brizitsky, G.V.Vinogradov, A.I.Isayev, Yu.Ya.Podolsky. *J. Appl. Polym. Sci.*, **21**, 751 (1977)
285. Y.Goutille, J.-Ch.Majeste, J.-F.Tassin, J.Guillet. *J. Non-Newton. Fluid Mech.*, **111,** 175 (2003)
286. D.R.Arda, M.R.Mackley. *J. Non-Newton. Fluid Mech.*, **126**, 47 (2005)
287. O.Kulikov, K.Hornung, M.Wagner. *Rheol. Acta*, **46**, 741 (2007)
288. R.Rutgers, M.Mackley. *J. Rheol.*, **44**, 1319 (2000)
289. S.-Q.Wang, N.Plucktaveesak. *J. Rheol.*, **43**, 453 (1999)
290. G.V.Vinogradov, L.I.Insarova, B.B.Boiko, E.K.Borisenkova. *Polym. Eng. Sci.*, **12,** 323 (1972)
291. Ph.J.Doerpringhaus, D.C.Baird. *Rheol. Acta*, **42**, 544 (2003)
292. M.Fernández, A.Santamaría, A.Muñoz-Escalona. L.Méndez. *J. Rheol.*, **45**, 595 (2001)
293. Zh.Zhu. *Rheol. Acta*, **43**, 373 (2004)
294. D.A.Hill, T.Hasegawa, M.M.Denn. *J. Rheol.*, **34**, 891 (1990)
295. H.J.Larrazabal, A.M.Hrymak, J.Vlachopoulos. *Rheol. Acta*, **45**, 705 (2006)
296. P.E.Boukany, P.Çapadia, S.-Q.Wang. *J. Rheol.*, **50**, 641 (2006)